Neuronal TIMP2 regulates hippocampus-dependent plasticity and extracellular matrix complexity

Ana Catarina Ferreira[1,2,3,4], Brittany M. Hemmer[1,2,3,4,5], Sarah M. Philippi[1,2,3,4,5], Hanxiao Liu[1,2,3,4], Jeffrey D. Zhu[1,2,3,4], Tatyana Kareva[1,2,3,4], Tim Ahfeldt[1,2,3,4], Merina Varghese[1], Patrick R. Hof[1,2], Joseph M. Castellano[1,2,3,4*]

[1]Nash Family Department of Neuroscience, Friedman Brain Institute, Icahn School of Medicine at Mount Sinai, New York, NY, United States

[2]Ronald M. Loeb Center for Alzheimer's Disease, Icahn School of Medicine at Mount Sinai, New York, NY, United States

[3]Department of Neurology, Icahn School of Medicine at Mount Sinai, New York, NY, United States

[4]Black Family Stem Cell Institute, Icahn School of Medicine at Mount Sinai, New York, NY, United States

[5]Graduate School of Biomedical Sciences, Icahn School of Medicine at Mount Sinai, New York, NY, United States

[*]Correspondence:

Joseph Castellano, Ph.D.

Icahn School of Medicine at Mount Sinai

1425 Madison Avenue, Box 1065

Phone: 212-659-5913

E-mail: joseph.castellano@mssm.edu

Running title: TIMP2 regulates hippocampal function through extracellular matrix

Abstract

The functional output of the hippocampus, a brain region subserving memory processes, depends on highly orchestrated cellular and molecular processes that regulate synaptic plasticity throughout life. The structural requirements of such plasticity and molecular processes involved in this regulation are poorly understood. Specific molecules, including tissue inhibitor of metalloproteinases-2 (TIMP2) have been implicated in processes of plasticity in the hippocampus, a role that decreases with brain aging as expression is lost. Here, we report that TIMP2 is highly expressed by neurons within the hippocampus and its loss drives changes in cellular programs related to adult neurogenesis and dendritic spine turnover with corresponding impairments in hippocampus-dependent memory. Consistent with the accumulation of ECM in the hippocampus we observe with aging, we find that TIMP2 acts to reduce accumulation of extracellular matrix (ECM) around synapses in the hippocampus. Moreover, its removal results in hindrance of newborn neuron migration through a denser ECM network. A novel conditional TIMP2 KO mouse reveals that neuronal TIMP2 regulates adult neurogenesis, accumulation of ECM, and ultimately hippocampus-dependent memory. Our results define a mechanism whereby hippocampus-dependent function is regulated by TIMP2 and its interactions with the ECM to regulate diverse processes associated with synaptic plasticity.

52 **Introduction**

53 A variety of cellular, molecular, and functional changes have now been documented in the brain
54 as aging progresses, leaving it susceptible to diseases like Alzheimer's disease. Given that aging
55 serves as the major risk factor for many neurological disorders, aging processes have increasingly
56 been considered to be valid therapeutic targets, especially as the aged population continues to
57 increase. Growing evidence in animal models indicates that the aged brain can be rejuvenated
58 through manipulation of the systemic environment, including through young plasma transfer or
59 sharing of young blood through heterochronic parabiosis[1-4]. Aged mice exposed to young blood
60 exhibit improved synaptic plasticity and cognitive performance[2]. We and others have begun to
61 identify factors present in young blood that confer brain rejuvenation phenotypes in aged mice[3,4].
62 Among those, we showed that tissue inhibitor of metalloproteinases-2 (TIMP2), a protein elevated
63 early in life, revitalizes function of the aged mouse hippocampus[4]. Despite demonstrating that this
64 factor is critical for young plasma-mediated memory improvements in aged mice[4], little is known
65 of the cellular and molecular details of how TIMP2 regulates function within the hippocampus.

66 TIMP2 is a secreted protein of approximately 21-kDa in size primarily known for its role in
67 regulating peripheral extracellular matrix (ECM) remodeling[5] through its unique dual roles in
68 regulating the activation of latent matrix metalloproteinases (MMPs), including MMP2, to
69 proteolytically active forms, and the inhibition of MMP activity[6,7]. Through these roles, TIMP2 has
70 been shown to play a key role in the maintenance of ECM network structure in many tissues with
71 myriad disease implications, including heart failure[8], cancer[9], and ischemic stroke[10], among
72 others. While early reports described expression of TIMP2 from development into adulthood[11],
73 and its role in regulating cortical neuronal differentiation[12] and subtle motor phenotypes[13], few
74 studies have examined the biological role of TIMP2 in the adult brain and how it modulates
75 function of the hippocampus. While we recently demonstrated that TIMP2 is critical in revitalizing
76 overall hippocampus-dependent cognitive function in aged mice[4], the biological role of TIMP2
77 expressed within the hippocampus has not been studied. TIMP2 is part of a small family of tissue

78 metalloproteinase inhibitors that include TIMP1, TIMP3, and TIMP4, all of which perform broad
79 MMP targeting functions but in diverse contexts in the brain, including in myelin repair[14],
80 neurovascular regulation[15], or in regulation of the tumor microenvironment[16]. Interestingly, TIMP2
81 shares only ~40-50% sequence homology with other TIMP family members and is particularly
82 expressed in the brain and enriched specifically in hippocampus relative to other TIMPs. Since
83 levels of TIMP2 decline in the hippocampus with age[4], understanding the function of this local
84 source will be important to understand its normal function and position it for putative therapies in
85 age-related brain disorders. Moreover, we sought to understand the extent to which ECM
86 regulation is related to disparate processes of plasticity to regulate complex behavioral outputs.
87 Here we define a mechanism by which TIMP2 regulates ECM components in the
88 hippocampus in a manner that regulates processes linked to plasticity and memory. We find that
89 TIMP2 is predominantly expressed by neurons in the hippocampus and is present at high levels
90 in the brain extracellular space adjacent to these cells. Deletion of TIMP2 induces transcriptomic
91 changes in the hippocampus that are consistent with processes related to synaptic plasticity and
92 adult neurogenesis. We find that loss of TIMP2 results in fewer dendritic spines in dentate gyrus
93 (DG) granule cells, decreased adult DG neurogenesis along several stages, and impaired
94 memory in various hippocampus-dependent tasks. Loss of TIMP2 also causes an accumulation
95 of ECM proteins, particularly around synapses within the DG, and impaired migration of
96 neuroblasts within the neurogenic niche, reflecting dysregulated ECM turnover and mimicking
97 ECM accumulation seen in the aged brain. Finally, we developed a mouse model for conditional
98 deletion of TIMP2 from neurons that exhibits the functional phenotypes observed in TIMP2 KO
99 mice, further arguing for a role of the neuronal pool of TIMP2 in shaping plasticity-related function
100 of the hippocampus. Our findings indicate molecular mechanisms through which neuronal TIMP2
101 remodeling of the ECM promotes synapse plasticity and is required for memory, with functional
102 implications for neurogenic rejuvenation.
103

Materials and Methods

See Supplementary Information for additional details.

Animals

All animal procedures were performed in accordance with the National Institutes of Health Guide for Care and Use of Laboratory Animals and the Icahn School of Medicine at Mount Sinai Institutional Animal Care and Use Committee. TIMP2 knockout (KO) (Jackson Laboratory) and WT female mice or $Syn^{Cre/+}$; $TIMP2^{fl/fl}$ and $TIMP2^{fl/fl}$ mice (generated as described in Supplementary Information) were used at 2-3 months or 5-6 months of age unless indicated otherwise. Littermate controls were used for all experiments. Mice were maintained on a 12-hour light/dark cycle at constant temperature (23°C) with *ad libitum* access to food and water.

Bulk RNA-sequencing

RNA-sequencing was performed on hippocampi dissected from WT and TIMP2 KO male and female mice. Quality of extracted RNA (RNeasy Mini Kit, Qiagen) was measured by Agilent TapeStation Bioanalyzer (Agilent Technologies), and all samples exhibited RNA Integrity Number (RIN) > 8. cDNA libraries were prepared with poly(A) selection and sequenced using Illumina Hiseq (2x150bp paired-end) (Genewiz). At least 25M clean reads were generated from each sample and mapped to the *Mus musculus* GRCm38 reference genome available on ENSEMBL, using STAR aligner (v.2.5.2b). After extraction of gene hit counts, the hit counts table was used for downstream differential expression analysis using DESeq2 software. The Wald test was used to generate *P*-values and log2 fold changes. Differentially expressed genes (DEGs; $P<0.05$) were used for Gene Set Enrichment Analysis (GSEA; https://www.gsea-msigdb.org/gsea/index.jsp). Volcano plot was generated with R v4.1.2.

Animal procedures

129 Mice were injected intraperitoneally (i.p.) once with 150 mg/kg of 5-bromo-2′-deoxyuridine (BrdU;
130 Sigma) 24 hours before sacrifice for cell proliferation assessment, or daily for 5 days, followed by
131 sacrifice/perfusion 28 days after initial injection for cell fate analysis. *In vivo* microdialysis
132 proceeded according to previous methods[17] with some adaptations (described in Supplementary
133 Information).
134
135 **Immunohistochemistry**
136 For all immunohistochemistry experiments, mice were anesthetized with a cocktail of ketamine
137 (90 mg/kg) and xylazine (10 mg/kg) and transcardially perfused with ice-cold 0.9% saline, and
138 brains were postfixed in 4% paraformaldehyde and preserved with 30% sucrose before sectioning
139 at 40-µm on a freezing-sliding microtome (SM2010R, Leica). Sections were incubated overnight
140 with indicated primary antibodies, followed by fluorescent secondary antibodies. Image
141 processing was performed with LSM 780 confocal microscope (Zeiss) using 40x/1.4 Oil DIC
142 objective. Four equally-spaced sections per mouse were used to count the total number of
143 positive cells within DG (subgranular zone and hilar subregions) using stereological principles. All
144 counts were performed using FIJI in a blinded fashion, according to similar methods[4].
145
146 **Aggrecan and Homer1 puncta quantification**
147 Quantification of the number of puncta by super-resolution microscopy proceeded according to
148 similar methods[18]. Images were acquired by confocal imaging using LSM 880 with AiryScan in
149 super-resolution mode (Zeiss) set with a 63X/1.4 Oil DIC objective with 5X optical zoom.
150 Aggrecan puncta were quantified with Puncta Analyzer plugin[19] in ImageJ, and thresholding was
151 applied equally across images. Colocalization of co-stained Aggrecan and Homer1 puncta was
152 analyzed with the Puncta Analyzer plugin with a minimum pixel specification of 4. Three images
153 in the molecular layer of the DG were averaged per mouse for analysis.
154

155 **Dendritic spine analysis by iontophoretic dye injections**

156 Tissue was processed according to similar work[20], and then coronal sections were incubated in
157 250 ng/ml DAPI to enable DG identification. Sections were mounted on nitrocellulose membrane
158 filters, immersed in ice-cold PB, and DG granule cells were iontophoretically injected with 5%
159 Lucifer Yellow (Invitrogen) under a direct current of 3-8 nA until the dye filled distal ends of the
160 dendrites, and then sections were mounted between spacers placed on gelatin-coated glass
161 slides (#22-214-320, Thermo Fisher). Images of dendritic segments from DG granule cells at the
162 suprapyramidal blade were acquired on a Zeiss LSM 780 confocal microscope using a 100x/1.46
163 Oil DIC M27 Plan-Apochromat objective, and stacks were acquired at 512 x 512-pixel resolution
164 with a Z-step of 0.1 µm, optical zoom of 3.3x, pinhole setting of 1 Airy Unit, and optimal settings
165 for gain and offset. Three z-stacks were imaged from each neuron. Confocal stacks were
166 deconvolved using an iterative blind deconvolution algorithm (AutoQuant X, vX3.0.1,
167 MediaCybernetics). Deconvolved stacks were analyzed using Neurolucida 360 (v2019.2.1; MBF
168 Bioscience) for semi-automated reconstruction to determine spine density and morphology.
169 Spines were classified as stubby, thin, mushroom, and filopodia, according to previous work[20,21].
170 4-5 mice per genotype, 6 neurons per mouse, and 3 dendrites per neuron were analyzed.

171

172 **Hippocampus-dependent behavior**

173 *Novel location recognition.* Mice were habituated to the open-field arena for 6 min, following
174 exposure to two different objects in fixed positions for three consecutive trials of 6 min each. On
175 day 2, mice explored the same arena with one object displaced to a novel position. Time spent
176 exploring each object was manually scored in a blinded fashion to assess the discrimination index
177 for the novel location.

178

179 *Contextual fear-conditioning.* Mice were trained using a 2-shock contextual fear conditioning
180 paradigm, as previously described[4]. Mice received two periods of 30 s consisting of a paired cue

light and a tone of 1,000-Hz, followed by a light foot-shock (2 s, 0.5 mA) separated by a 180-s interval (light foot-shock; Ugo Basile). Twenty-four hours later, mice were re-exposed to the same context for 3 min, and freezing levels (contextual) were measured using EthoVision XT system software (v14.0.1319, Noldus).

Barnes maze. Mice were tested on a large circular Barnes maze in which mice navigate using visual cues to an alternating escape hole over four trials on each day of the task, as described[4]. Search strategy classification was manually performed based on methods adapted from previous work[22], categorized as localized, serial, random, scanning, focal, focal missense, targeted and direct. Each related strategy was categorized into non-hippocampus-dependent strategies (localized, serial, random, and scanning), and hippocampus-dependent strategies (focal, focal missense, targeted and direct). Cognitive performance of each trial on day 3 was scored according to the following, with a separation of 1 point between non-hippocampus-dependent and hippocampus-dependent strategies to account for additional cognitive complexity: localized=0, serial=1, random=2, scanning=3, focal=5, focal missense=5, targeted=6, direct=6. Focal and focal missense strategies are assigned “5”, as both are goal-directed strategies used without achieving the final target. Target and direct strategies were assigned “6” since both are goal-directed strategies with successful achievement of the final target.

Statistical analysis

Statistical analyses were performed using GraphPad Prism version 9.0 software (GraphPad Software) using tests described in text and figure legends, including student’s *t* test for 2-group comparisons, nested *t* tests with multi-level variables for 2-group comparisons, or chi-square analysis for 2-group comparisons of proportions. All experiments were performed in a randomized and blinded fashion.

207 **Results**

208 **TIMP2 is expressed in hippocampal neurons, and its deletion induces transcriptomic**
209 **changes**

210 TIMP2 exhibits high expression in the hippocampus relative to other brain regions[4]. To identify
211 the cellular sources of TIMP2 in the hippocampus and to begin to probe its function in this region,
212 we examined TIMP2 protein levels by confocal microscopy in various subfields of the
213 hippocampus of 2-month-old wildtype (WT) male and female mice. We found that TIMP2 is
214 expressed in the hilus of dentate gyrus (DG), as well as CA3 and CA1 subfields of the
215 hippocampus, and we found that the majority of TIMP2-expressing cells also stain for pan-
216 neuronal marker, NeuN, arguing that the major cellular source of TIMP2 expression in these areas
217 was neuronal (**Fig. 1A, 1B**). We did not detect differential TIMP2 neuronal expression in the
218 hilus/DG, CA3, and CA1 subfields between males and females (**Supplementary Fig. 1A-C**).

219 Given the high level of TIMP2 expression seen in neurons in the hippocampus, we asked
220 whether levels were elevated in the extracellular space adjacent to this cellular source. To
221 measure extracellular levels of TIMP2 in this region, we implanted high molecular-weight cut-off
222 (1-MDa) probes into hippocampi of freely moving, 2-3-month-old WT mice to measure interstitial
223 fluid (ISF) levels of TIMP2 by *in vivo* microdialysis. TIMP2 was readily detectable in the ISF in
224 hippocampus (**Fig. 1D**), and extrapolated values of exchangeable ISF TIMP2 were ~10.1 ± 0.16
225 ng/mL (N=3), as measured at a flow rate of 1 µl/min. Importantly, the 21- to 22-kDa TIMP2 band
226 was absent in the ISF of hippocampus from mice in which TIMP2 has been deleted (KO) (**Fig.**
227 **1D**).

228 The high levels of TIMP2 within neurons and the extracellular space of the hippocampus
229 argues for unappreciated roles for its function locally in this region, prompting us to examine the
230 cellular and molecular processes regulated by TIMP2. In order to identify putative pathways
231 involved in TIMP2 function in the hippocampus, we isolated hippocampi from WT and TIMP2 KO
232 male and female mice and processed the tissue for RNA-sequencing (**Fig. 1E**). A total of 905

233 differentially expressed genes (DEGs; *P<0.05*) were identified in TIMP2 KO compared to WT (**Fig.**
234 **1F**), with TIMP2 being the top DEG, as expected. Of these genes, 449 DEGs were downregulated
235 in TIMP2 KO hippocampi (**Fig. 1F**). To gain insights into how the altered transcriptome may reflect
236 altered biological processes, we performed gene set enrichment analysis (GSEA).
237 Downregulated DEGs in TIMP2 KO were enriched for a number of Gene Ontology (GO) biological
238 processes related to plasticity, including "cell morphogenesis", "neurogenesis", "cell projection
239 organization", and "synapse organization" (**Fig. 1G**). Upregulated DEGs in TIMP2 KO were
240 enriched in functions that included "regulation of cell death and cell cycle", among others
241 (**Supplementary Fig. 1E**). Together, our data suggest that TIMP2 in the normal hippocampus
242 may be involved in processes of plasticity.
243
244 **TIMP2 is necessary for adult neurogenesis in the normal dentate gyrus**
245 To evaluate the extent to which our discovery-based pathway approach from RNAseq highlighted
246 processes that may indeed be regulated by TIMP2, we examined the key cellular processes
247 implicated. As one of the top downregulated pathways in hippocampus of TIMP2 KO vs. WT mice
248 was "neurogenesis", we used confocal microscopy to begin to address whether adult
249 neurogenesis processes within the DG are indeed altered by absence of TIMP2. To examine
250 whether TIMP2 regulates overall cell proliferation, we injected WT and TIMP2 KO mice with the
251 proliferation marker bromodeoxyuridine (BrdU), which labels the pool of proliferating cells in the
252 subgranular zone (SGZ) of DG (**Fig. 2A**). We found that the DG of TIMP2 KO mice had
253 significantly fewer proliferating cells than in WT mice (**Fig. 2C)**, as quantified by the total number
254 of $BrdU^+$ cells (**Fig. 2D**). We observed a similar result when analyzing the pool of $Ki67^+$ cells in
255 the SGZ (**Fig. 2E-F**), which marks a larger pool of proliferating cells in other phases. We next
256 analyzed the pool of neural progenitor cells and the immature neuroblasts they ultimately give
257 rise to, using SRY-Box Transcriptional Factor 2 (Sox2) and doublecortin (DCX) as markers,

258 respectively. Deletion of TIMP2 resulted in a significant decrease in the number of Sox2$^+$ neural
259 progenitor cells (**Fig. 2G-H**), and of DCX$^+$ immature neurons (**Fig. 2I-J**).
260 To examine whether this disrupted pool of neuroblasts corresponds to a differing number
261 of surviving immature neurons, we injected TIMP2 KO and WT mice by pulse-chase labeling with
262 BrdU for 5 days and quantified the number of label-retaining, surviving BrdU$^+$ NeuN$^+$ neurons in
263 the SGZ of DG 4 weeks later (**Fig. 2B**). Using this paradigm, we found that the DG of TIMP2 KO
264 mice had significantly fewer newborn neurons compared with the DG of WT mice (**Fig. 2K-L**).
265 Together, these results are consistent with TIMP2-mediated roles in adult neurogenesis and
266 related pathways uncovered by our transcriptomic analysis.
267
268 **TIMP2 regulates dendritic spine plasticity in the dentate gyrus**
269 Our transcriptomic data in TIMP2 KO hippocampi suggest a role for TIMP2 acting within the
270 hippocampus to modulate plasticity processes, including "synapse organization", possibly at the
271 structural level. To evaluate the impact of TIMP2 deletion on dendritic spines, the cellular
272 substrates of memory storage[23], we turned to a rigorous method to sensitively quantify dendritic
273 spines and classify them. We performed Lucifer Yellow iontophoretic dye-filling of mature DG
274 granule cells in isolated slices from TIMP2 KO and WT mice for high-resolution imaging and
275 reconstruction (**Fig. 3A**)[21,24]. We found that neurons in the DG of TIMP2 KO mice exhibited
276 significantly reduced dendritic spine density compared to those in WT DG (**Fig. 3B, E**). We then
277 used automated classification algorithms[21,25] to classify and quantify spines based on
278 morphology, as a readout of spine plasticity. Intriguingly, we found a significantly higher proportion
279 of immature thin spines in labeled DG neurons from TIMP2 KO mice compared to those in WT
280 mice (**Fig. 3C, E**) and a significantly decreased proportion of mature mushroom spines (**Fig. 3D,
281 E**) exhibited by TIMP2 KO relative to WT DG neurons. Mushroom spines are a particularly stable
282 class of spines with lower turnover[26] and are proposed to serve as structural correlates of
283 memory[27]. Of note, our observations of spines in DG neurons of TIMP2 KO mice are in line with

284 previous descriptions of altered synaptic function upon TIMP2 modulation[4], including long-term
285 potentiation, which was shown to be affected by modulating levels of TIMP2[4]. Collectively, these
286 results suggest that TIMP2 may act to promote plasticity through regulation of adult neurogenesis
287 and dendritic spine formation.
288
289 **TIMP2 is required for hippocampus-dependent memory function**
290 The hippocampus is critical for spatial memory and learning, likely through regulation of adult
291 neurogenesis in the DG (reviewed in[28]), as well as through changes in synaptic structure[29,30]. The
292 changes we observed in both adult neurogenesis and dendritic spine plasticity in TIMP2 KO
293 hippocampi prompted us to investigate whether TIMP2 is involved in hippocampus-dependent
294 memory and learning. We first utilized the novel location recognition task (**Fig. 4A**), in which mice
295 use spatial cues in the arenas to learn and associate the positions of objects in space. Twenty-
296 four hours after training, we observed that TIMP2 KO mice exhibited significantly decreased
297 preference for the training object when displaced, as indicated by the reduced discrimination index
298 (**Fig. 4B**), thus suggesting a critical role of TIMP2 in spatial memory in healthy mice. We next
299 employed contextual and cued fear-conditioning to evaluate whether the mice differ in the ability
300 to discriminate the previously aversive training context or a new cue-driven context (**Fig. 4C**).
301 Assessment of context discrimination revealed significantly reduced freezing behavior by TIMP2
302 KO mice, suggesting impaired hippocampus-associated contextual discrimination in the absence
303 of TIMP2 (**Fig. 4D-E**), while amygdala-associated cued freezing levels were unchanged
304 (**Supplementary Fig. 2A**). We next examined whether more complex hippocampus-dependent
305 spatial memory was altered in a Barnes maze assay in which mice use a variety of strategies
306 while navigating an illuminated maze surface to an escape hole using spatial cues. Strategies
307 were divided into non-hippocampus-dependent and hippocampus-dependent with increasing
308 levels of cognitive demand (**Fig. 4F**)[22]. Analysis of the strategies used to reach the escape hole
309 revealed that TIMP2 KO mice delayed the switch from non-hippocampal-dependent to

310 hippocampal-dependent strategies while performing the task (**Fig. 4G**). On day 3 of the Barnes
311 maze, a significant lower proportion of TIMP2 KO mice used hippocampus-dependent strategies
312 compared to WT mice (**Fig. 4H**). Further categorization of cognitive performance by scoring the
313 different strategies according to level of complexity related to spatial learning[31] showed that
314 TIMP2 KO mice achieved significantly lower cognitive scores relative to WT mice (**Fig. 4I**),
315 consistent with impaired hippocampus-dependent function in TIMP2 KO mice while performing in
316 the Barnes maze.

317 Importantly, we did not detect differences in motor function and overall activity in TIMP2
318 KO mice (**Supplementary Fig. 2B-J**). Motor coordination perturbations have been reported in
319 TIMP2 mutant mice[13], so we subjected the mice to a wide battery of motor function, coordination,
320 and activity assays, including rotarod, open field, wire testing, pole testing, grip strength, none of
321 which revealed changes in corresponding function between TIMP2 KO and WT mice
322 (**Supplementary Fig. 2B-I**). We detected impaired clasping behavior in TIMP2 KO relative to WT
323 mice (**Supplementary Fig. 2J**), as previously reported[13], but this form of motor coordination does
324 not impact performance observed for TIMP2 KO mice in the wide range of hippocampus-
325 dependent tasks utilized. No differences in anxiety-related behaviors in the open field were
326 observed between WT and TIMP2 KO mice (**Supplementary Fig. 2F**). Collectively, these results
327 indicate a critical role for TIMP2 in regulation of hippocampus-dependent memory.

328

329 **TIMP2 ablation leads to accumulation of ECM in the hippocampus**

330 We next investigated potential mechanisms that may account for how spine formation and adult
331 DG neurogenesis are regulated by TIMP2. Outside the brain, TIMP2 has been characterized to
332 be involved in ECM degradation and remodeling through its canonical binding partner MMP2[6,7].
333 Brain ECM is dynamic, and accumulating evidence suggests a role for ECM and its components
334 in the regulation of synaptic plasticity, including in spine remodeling[18,32], adult neurogenesis[33],
335 and cognition[33]. We first assessed the levels of pro-MMP2 in lysates of hippocampi from TIMP2

336 KO and WT mice. Interestingly, we found significantly elevated levels of MMP2, both at the gene
337 (**Fig. 5A**) and protein (**Fig. 5B-C**) levels in the absence of TIMP2, reflecting an accumulation in
338 response to loss in TIMP2 signaling and pointing to a potential disruption in ECM remodeling and
339 turnover in hippocampus.

340 Recent work indicates that brain ECM levels increase with age in parallel with age-
341 dependent cognitive decline[34]. In the brain, chondroitin sulfate proteoglycans (CSPGs) are the
342 major class of ECM proteins[35,36]. The proteoglycan aggrecan, a core CSPG expressed in
343 perineuronal nets in the brain, is highly enriched in the ECM of the DG[37] and has been linked to
344 synaptic plasticity[38] and memory[39,40]. Using super-resolution confocal imaging, we find that
345 aggrecan is significantly increased in the hippocampus of aged mice (**Fig. 5 D-E**), a change that
346 occurs alongside the progressive decrease in TIMP2 expression[4]. We therefore analyzed
347 aggrecan distribution in the hippocampus of young WT and TIMP2 KO mice and found that TIMP2
348 KO mice exhibited a significant increase in the density of aggrecan puncta in the DG molecular
349 layer (**Fig. 5D-E**), the same area where we observed impaired spine remodeling in TIMP2 KO
350 relative to WT mice (**Fig. 3**). To further determine if TIMP2 remodeling of the ECM could affect
351 accumulation of ECM near synapses given the synaptic deficits we observed in these neurons,
352 we analyzed aggrecan colocalization with the postsynaptic protein Homer1. We observed that the
353 DG of TIMP2 KO mice exhibited significantly increased colocalization of aggrecan with Homer1
354 relative to that observed in WT DG (**Fig. 5F-G**). These data indicate that TIMP2 normally promotes
355 ECM remodeling and limits its deposition near synapses.

356 We next further characterized the relationship between TIMP2's effect on ECM and adult
357 neurogenesis, considering the known roles of ECM and its related components in the regulation
358 of proliferation and migration of newborn neurons (reviewed in[41]). To explore this possibility, we
359 evaluated the migration of newborn neurons toward the molecular layer by examining the
360 distribution of DCX^+ immature neuroblasts in the SGZ relative to that in the GCL of the DG. This
361 analysis revealed significantly decreased distribution of DCX^+ immature neurons in the GCL of

362 TIMP2 KO mice (**Fig. 5H-I**), reflecting a process whereby migration of newborn neurons within
363 the DG is apparently impaired in the absence of TIMP2. These data suggest that the absence of
364 TIMP2 leads to a tighter ECM structural environment that acts to spatially restrict the migration of
365 newborn neurons and plasticity of synapses, thus affecting overall adult neurogenesis and spine
366 dynamics. In support of this concept, we measured structural changes in the ECM of TIMP2 KO
367 mice by performing surface scanning electron microscopy (SEM) on decellularized brains isolated
368 from TIMP2 KO and WT mice. Interestingly, we detected altered ECM microarchitecture in the
369 form of thicker ECM fibers (**Fig. 5J-K**) in hippocampi from TIMP2 KO compared to WT mice.
370 Together, our results suggest that TIMP2 modulates the flexibility of the ECM within the
371 hippocampus to regulate plasticity processes, including adult neurogenesis and spine plasticity.
372

373 **Neuronal TIMP2 regulation of the extracellular matrix regulates hippocampus-dependent**
374 **cognitive function and adult neurogenesis**

375 To gain further mechanistic insight into TIMP2's role in the function of the hippocampus with
376 increased cellular resolution, we generated *Timp2*-floxed (TIMP2$^{fl/fl}$) mice using two-cell
377 homologous recombination (2C-HR)-CRISPR/Cas9-based genome editing. We inserted two
378 *loxP* sites flanking exon 2 of the *Timp2* gene transcript (**Supplementary Fig. 3A-B**) and then
379 crossbred *Timp2*$^{fl/fl}$ mice with Syn$^{Cre/+}$ mice (**Supplementary Fig. 3C**) to specifically excise *Timp2*
380 in neurons. Immunoblotting against TIMP2 from isolated hippocampus lysates of Syn$^{Cre/+}$;
381 TIMP2$^{fl/fl}$ or TIMP2$^{fl/fl}$ control mice confirmed that conditional targeting of TIMP2 resulted in
382 significantly reduced TIMP2 levels compared to TIMP2$^{fl/fl}$ controls in hippocampus
383 (**Supplementary Fig. 3D-E**). We performed further validation by performing confocal microscopy
384 in hippocampus of Syn$^{Cre/+}$; TIMP2$^{fl/fl}$ or TIMP2$^{fl/fl}$ control mice to examine the cells in hippocampus
385 expressing TIMP2. Quantification of TIMP2^{+} NeuN^{+} cells in the hilus/DG, CA3 and CA1 regions
386 revealed significant abrogation of TIMP2 in neurons upon its conditional deletion (**Supplementary**
387 **Fig. 3F-G**). These data validate our model as a tool for addressing the role of neuronal TIMP2 in

388 regulating the key cellular and behavioral phenotypes observed in the context of global TIMP2
389 deletion.

390 Given that we found that TIMP2 was expressed by neurons in DG and present at
391 significant levels in the extracellular space adjacent to these cells, we sought to determine
392 whether the pool of neuronal TIMP2 is specifically involved in hippocampus-dependent memory.
393 Using the Syn$^{Cre/+}$; TIMP2$^{fl/fl}$ mice we generated and validated (**Supplementary Fig. 3**), we
394 created cohorts of Syn$^{Cre/+}$; TIMP2$^{fl/fl}$ mice and TIMP2$^{fl/fl}$ control littermates to evaluate performance
395 in spatial memory tasks. We found that Syn$^{Cre/+}$; TIMP2$^{fl/fl}$ mice exhibited significantly decreased
396 preference for the displaced object 24 hours after training in the testing phase compared to
397 TIMP2$^{fl/fl}$ controls, as indicated by a reduced discrimination index in these mice (**Fig. 6A**). Further
398 assessment in the contextual portion of fear-conditioning revealed a significant reduction in
399 freezing levels by Syn$^{Cre/+}$; TIMP2$^{fl/fl}$ mice compared to TIMP2$^{fl/fl}$ controls, suggesting impaired
400 contextual memory in the absence of neuronal TIMP2 (**Fig. 6B-C**). Cued freezing levels were
401 indistinguishable between the groups of mice (**Supplementary Fig. 4A**). We then subjected the
402 mice to Barnes maze testing to examine performance in search strategies to find the escape hole.
403 Our search strategy analysis showed that a smaller proportion of Syn$^{Cre/+}$; TIMP2$^{fl/fl}$ mice used
404 hippocampus-dependent strategies compared to TIMP2$^{fl/fl}$ mice (**Fig. 6D-E**). Scoring their search
405 strategy utilization by complexity shows that Syn$^{Cre/+}$; TIMP2$^{fl/fl}$ mice score lower than their
406 TIMP2$^{fl/fl}$ counterparts (**Fig. 6F**), suggesting TIMP2 from neurons is required for normal
407 hippocampus-related memory and learning. Importantly, we did not detect differences in overall
408 motor function in terms of coordination (**Supplementary Fig. 4B-C**), overall activity in the open
409 field (**Supplementary Fig. 4D-E**), grip strength or motor learning (**Supplementary Fig. 4G-I**) and
410 clasping behavior (**Figure S3J**) in Syn$^{Cre/+}$; TIMP2$^{fl/fl}$ mice relative to TIMP2$^{fl/fl}$ mice. No differences
411 in anxiety-related behaviors in the open field were observed between TIMP2$^{fl/fl}$ and Syn$^{Cre/+}$;
412 TIMP2$^{fl/fl}$ mice (**Supplementary Fig. 4F**).

413 To test whether the local pool of neuronal TIMP2 affects the survival of newly generated
414 neurons, we analyzed the pool of $BrdU^+$ $NeuN^+$ cells after pulse-chase labeling with BrdU, as
415 described earlier (**Fig. 2B**). Indeed, we observed that the deletion of TIMP2 within neurons
416 resulted in a significant decrease in the number of $BrdU^+$ $NeuN^+$ newborn neurons compared to
417 $TIMP2^{fl/fl}$ controls (**Fig. 6G-H**). To probe potential mechanisms by which TIMP2 expressed locally
418 from neurons affects hippocampus-dependent memory and adult neurogenesis, we next
419 addressed ECM-related remodeling in the DG of $Syn^{Cre/+}$; $TIMP2^{fl/fl}$ mice. TIMP2 deletion in
420 neurons in $Syn^{Cre/+}$; $TIMP2^{fl/fl}$ mice resulted in a significant increase in the density of aggrecan-
421 positive puncta compared to $TIMP2^{fl/fl}$ controls (**Fig. 6I-J**), as well as increased colocalization of
422 aggrecan with Homer1 (**Fig. 6I, 6K**), consistent with an accumulation of ECM components
423 adjacent to synapses, as observed earlier. Together, our results show that the pool of neuronal
424 TIMP2 is necessary to promote ECM remodeling to enable synaptic plasticity and adult
425 neurogenesis to facilitate normal hippocampus-dependent memory.
426

427 **Discussion**

428 Our study illustrates how alterations in the ECM within the hippocampus by TIMP2 can directly
429 regulate features of plasticity, including dendritic spine plasticity, adult neurogenesis, and
430 hippocampus-dependent memory. We find that TIMP2 is highly expressed in neurons within the
431 hippocampus and found at high levels in the brain extracellular space. Its removal induces
432 structural synaptic changes and deficits in adult neurogenesis, as predicted from changes
433 observed at the transcriptomic level, both of which result in impairments in hippocampus-
434 dependent memory function. We demonstrate that TIMP2's role in ECM remodeling is associated
435 with changes in the flexibility of synaptic plasticity, impinging on processes like neuronal migration
436 and differentiation. We generate and characterize a novel mouse model for conditional deletion
437 of TIMP2 within neurons, highlighting molecular mechanisms through which neuronal TIMP2
438 promotes synaptic plasticity through regulation in the ECM to facilitate normal memory.

439 The development and maintenance of synapses is critical in the establishment of
440 functional neuronal circuits, and emerging evidence indicates a role for the ECM and its
441 components in regulating synapse structure and morphology[41-43]. We used high-resolution
442 imaging of labeled granule cells in the intact hippocampus of TIMP2 KO and WT mice to show
443 that TIMP2 regulates dendritic spine density, with a loss in KO mice in the class of spines involved
444 in memory, mushroom spines[26]. Moreover, when TIMP2 is targeted either globally or specifically
445 within neurons, ECM components like aggrecan accumulate around hippocampal synapses, and
446 the ECM is more dense, as shown by our SEM data, suggesting that TIMP2 acts directly within
447 the hippocampus to modulate plasticity on a structural level. In agreement with its role in
448 modulating plasticity, we also find that TIMP2 regulates the process of adult neurogenesis. While
449 immature neuroblasts were unaltered in mice with systemic modulation of TIMP2[4], presumably
450 due to the window over which TIMP2 was modulated being too short to reflect changes in DCX^+
451 cells, we now show that removal of TIMP2, both globally and from neurons in the hippocampus,
452 results in disruption in neural progenitor proliferation and maturation. This is in line with *in vitro*
453 evidence indicating that TIMP2 expression was significantly upregulated upon neuronal
454 differentiation[44], and that it may be involved in differentiation[12]. Intriguingly, we observed that
455 TIMP2 deletion affected the migration of immature DCX^+ neurons towards the molecular layer,
456 arguing for a role of ECM in regulating neuronal migration[45]. It has been documented that ECM
457 molecules participate in neurogenesis[41], though the mechanisms by which they regulate neuronal
458 differentiation are unclear. CSPGs are known to surround new neurons in the hippocampus and
459 have recently been shown to be important in the production of new neurons[33], and ECM-related
460 proteins like reelin also play critical roles in neuronal migration[45].
461
462 TIMP2 is traditionally recognized for its unique dual role in regulating both the activation
463 of pro-MMP2 and the inhibition of MMP2 activity necessary for ECM remodeling[6,7]. We observed
464 that deletion of TIMP2 increased levels of *Mmp2* and pro-MMP2 levels within hippocampus,

465 perhaps reflecting compensatory responses to reduced TIMP2 and impaired MMP2 activation, as
466 described outside of the brain[6,7]. Accumulated pro-MMP2 appears to translate to less remodeling
467 of the ECM and its resulting accumulation around cells of the DG neurogenic niche we observe.
468 A proposed mechanism of spine stabilization and remodeling by ECM includes a structural-spatial
469 restriction mechanism in which ECM components, including CSPGs, form a matrix around
470 dendritic spines to provide extracellular rigidity and physically restrict spine motion[46]. MMPs
471 themselves can modulate structural plasticity by loosening the ECM structure, allowing for a more
472 permissive environment[41]. Moreover, stiffness of the surrounding environment determined by
473 ECM complexity has been implicated in regulating cell migration[47,48], including for neural stem
474 cells *in vitro*[49-51]. This modulation has been proposed to be among fundamental cell fate-
475 determining factors in neural development and neurological disorders[52-54]. Our results argue that
476 ECM accumulation in the absence of TIMP2 leads to a denser network that creates physical
477 restrictions that impact turnover of synapses from thin into mature mushroom-shaped spines,
478 while impeding proliferation and migration related to adult neurogenesis.

479 In line with reports linking disrupted synaptic plasticity and neurogenesis with cognitive
480 dysfunction[41], we show that TIMP2-related changes in hippocampus plasticity create significant
481 memory impairments. Both global and neuron-specific targeting of TIMP2 levels leads to deficits
482 in hippocampus-dependent memory tasks. Our results strongly reinforce a surprising link among
483 TIMP2, synaptic plasticity, and memory in the healthy hippocampus through regulating spine
484 dynamics and neurogenesis. Importantly, the cognitive phenotypes described here cannot be
485 attributed to TIMP2's role in other brain regions related to motor function, though earlier work in
486 younger mice described subtle deficits in coordination upon TIMP2 deletion[13], primarily related to
487 cerebellar alterations deletion[13]. We show that TIMP2-mediated roles in ECM to regulate cellular
488 phenotypes are associated with changes in MMP2. TIMP2 likely interacts with many MMPs and
489 other binding partners to mediate functional changes under different conditions, including
490 alpha3beta1 integrin[12]. It is possible that TIMP2 exerts its diverse biological functions through

491 interactions with different binding partners, or that it exerts its activities differently *in vivo* versus
492 *in vitro*, all of which will need to be further explored in future studies. Moreover, while we mostly
493 find TIMP2 expressed in neurons in our study, its expression in other cell types may be important
494 in certain pathological contexts[55] to be explored further, especially as a role for microglia in
495 remodeling the ECM to promote synapse plasticity in the hippocampus has been recently
496 described[18].

497 Dysregulation of the ECM is implicated in cognitive dysfunction that occurs in aging[56] and
498 in disease[57]. The progressive decline in TIMP2 expression with age[4] occurs in parallel with deficits
499 in memory[58] and ECM accumulation, as demonstrated here, while systemic treatment with TIMP2
500 revitalizes hippocampus-related function in aged mice[4]. Moreover, ECM clearance is beneficial in
501 mouse models of Alzheimer's disease pathology[59]. It has been increasingly appreciated that adult
502 neurogenesis in the human DG is dysregulated in Alzheimer's disease[60]. Defining the precise
503 molecular mechanisms accounting for how modulators of the ECM regulate the healthy brain may
504 lead to development of novel approaches for cognitive repair in contexts of aging or
505 neurodegeneration.

506

507 **Acknowledgments**

508 We gratefully acknowledge the contributions of the Mouse Genetics and Gene Targeting (MGGT)
509 CoRE facility (Kevin Kelley, ISMMS), which is supported by ISMMS and the National Cancer
510 Institute of the NIH under award P30CA196521, for two-cell stage embryo microinjections for
511 generating TIMP2$^{fl/fl}$ mice. We also thank Chingwen Yang of the CRISPR and Genome Editing
512 Center (Rockefeller University) for assistance generating constructs to develop the TIMP2$^{fl/fl}$ line.
513 We thank Yihang Wang (ISMMS) for RNA isolation support, Nikos Tzavaras and Deanna Benson
514 of the Microscopy CoRE and Advanced Bioimaging Center (ISMMS) for advice and equipment
515 for Airyscan microscopy and image analysis, Lee Cohen-Gould of the Electron Microscopy &
516 Histology Services of Weill Cornell Medicine Microscopy & Image Analysis Core for SEM sample

517 preparation, Jorge Morales of the Microscopy Facility (CCNY) for SEM acquisition support, and
518 Ron Gordon and Andy Leonard of the EM Core (ISMMS) for advice and sample preparation for
519 SEM. This work was funded by the National Institute on Aging (R01AG061382 (J.M.C),
520 RF1AG072300 (J.M.C.), T32AG049688 (B.M.H.), and R01AG061382-02S1 (J.M.C., S.M.P)).
521

522 **Author contributions**

523 A.C.F. and J.M.C. conceived and designed the experiments, performed data analysis and
524 interpretation, and wrote the manuscript. A.C.F. conducted the experiments. B.M.H. performed
525 and analyzed microdialysis experiments. S.M.P analyzed data for RNAseq experiments. H.L. and
526 J.D.Z performed or analyzed motor or Barnes maze experiments. M.V. performed intracellular
527 dye injections for spine labeling, and analyzed/interpreted data with P.R.H. T.K. and T.A. assisted
528 with design and analysis of $TIMP2^{fl/fl}$ validation data. All authors approved the final manuscript.
529

530 **Conflict of interests**

531 J.M.C. is listed as a co-inventor on patents for treating aging-associated conditions, including the
532 use of young plasma administration (US10688130B2) or youth-associated protein TIMP2
533 (US10617744B2), the latter of which is licensed to Alkahest, Inc.
534

535 *Supplementary Materials and Methods and Supplementary Figures are available at the end of*
536 *the document.*
537

538 **References**

539 1. Villeda SA, Luo J, Mosher KI, Zou B, Britschgi M, Bieri G *et al.* The ageing systemic milieu
540 negatively regulates neurogenesis and cognitive function. *Nature* 2011; **477**(7362)**:** 90-
541 94.
542
543 2. Villeda SA, Plambeck KE, Middeldorp J, Castellano JM, Mosher KI, Luo J *et al.* Young
544 blood reverses age-related impairments in cognitive function and synaptic plasticity in
545 mice. *Nat Med* 2014; **20**(6)**:** 659-663.
546
547 3. Katsimpardi L, Litterman NK, Schein PA, Miller CM, Loffredo FS, Wojtkiewicz GR *et al.*
548 Vascular and neurogenic rejuvenation of the aging mouse brain by young systemic
549 factors. *Science* 2014; **344**(6184)**:** 630-634.
550
551 4. Castellano JM, Mosher KI, Abbey RJ, McBride AA, James ML, Berdnik D *et al.* Human
552 umbilical cord plasma proteins revitalize hippocampal function in aged mice. *Nature* 2017;
553 **544**(7651)**:** 488-492.
554
555 5. Brew K, Nagase H. The tissue inhibitors of metalloproteinases (TIMPs): an ancient family
556 with structural and functional diversity. *Biochim Biophys Acta* 2010; **1803**(1)**:** 55-71.
557
558 6. Caterina JJ, Yamada S, Caterina NC, Longenecker G, Holmback K, Shi J *et al.* Inactivating
559 mutation of the mouse tissue inhibitor of metalloproteinases-2(Timp-2) gene alters
560 proMMP-2 activation. *J Biol Chem* 2000; **275**(34)**:** 26416-26422.
561
562 7. Wang Z, Juttermann R, Soloway PD. TIMP-2 is required for efficient activation of proMMP-
563 2 in vivo. *J Biol Chem* 2000; **275**(34)**:** 26411-26415.

564

565 8. Kandalam V, Basu R, Moore L, Fan D, Wang X, Jaworski DM *et al.* Lack of tissue inhibitor
566 of metalloproteinases 2 leads to exacerbated left ventricular dysfunction and adverse
567 extracellular matrix remodeling in response to biomechanical stress. *Circulation* 2011;
568 **124**(19)**:** 2094-2105.
569

570 9. Kaczorowska A, Miekus N, Stefanowicz J, Adamkiewicz-Drozynska E. Selected Matrix
571 Metalloproteinases (MMP-2, MMP-7) and Their Inhibitor (TIMP-2) in Adult and Pediatric
572 Cancer. *Diagnostics (Basel)* 2020; **10**(8).
573

574 10. Guo T, Hao H, Zhou L, Zhou F, Yu D. Association of SNPs in the TIMP-2 gene and large
575 artery atherosclerotic stroke in southern Chinese Han population. *Oncotarget* 2018; **9**(4)**:**
576 4698-4706.
577

578 11. Fager N, Jaworski DM. Differential spatial distribution and temporal regulation of tissue
579 inhibitor of metalloproteinase mRNA expression during rat central nervous system
580 development. *Mech Dev* 2000; **98**(1-2)**:** 105-109.
581

582 12. Perez-Martinez L, Jaworski DM. Tissue inhibitor of metalloproteinase-2 promotes
583 neuronal differentiation by acting as an anti-mitogenic signal. *J Neurosci* 2005; **25**(20)**:**
584 4917-4929.
585

586 13. Jaworski DM, Soloway P, Caterina J, Falls WA. Tissue inhibitor of metalloproteinase-
587 2(TIMP-2)-deficient mice display motor deficits. *J Neurobiol* 2006; **66**(1)**:** 82-94.
588

589 14. Nicaise AM, Johnson KM, Willis CM, Guzzo RM, Crocker SJ. TIMP-1 Promotes
590 Oligodendrocyte Differentiation Through Receptor-Mediated Signaling. *Mol Neurobiol*
591 2019; **56**(5)**:** 3380-3392.
592
593 15. Dewing JM, Carare RO, Lotery AJ, Ratnayaka JA. The Diverse Roles of TIMP-3: Insights
594 into Degenerative Diseases of the Senescent Retina and Brain. *Cells* 2019; **9**(1).
595
596 16. Solga R, Behrens J, Ziemann A, Riou A, Berwanger C, Becker L *et al.* CRN2 binds to
597 TIMP4 and MMP14 and promotes perivascular invasion of glioblastoma cells. *Eur J Cell*
598 *Biol* 2019; **98**(5-8)**:** 151046.
599
600 17. Ulrich JD, Burchett JM, Restivo JL, Schuler DR, Verghese PB, Mahan TE *et al.* In vivo
601 measurement of apolipoprotein E from the brain interstitial fluid using microdialysis. *Mol*
602 *Neurodegener* 2013; **8:** 13.
603
604 18. Nguyen PT, Dorman LC, Pan S, Vainchtein ID, Han RT, Nakao-Inoue H *et al.* Microglial
605 Remodeling of the Extracellular Matrix Promotes Synapse Plasticity. *Cell* 2020; **182**(2)**:**
606 388-403 e315.
607
608 19. Ippolito DM, Eroglu C. Quantifying synapses: an immunocytochemistry-based assay to
609 quantify synapse number. *J Vis Exp* 2010; (45).
610
611 20. Jacot-Descombes S, Keshav NU, Dickstein DL, Wicinski B, Janssen WGM, Hiester LL *et*
612 *al.* Altered synaptic ultrastructure in the prefrontal cortex of Shank3-deficient rats. *Mol*
613 *Autism* 2020; **11**(1)**:** 89.
614

615 21. Dickstein DL, Dickstein DR, Janssen WGM, Hof PR, Glaser JR, Rodriguez A *et al.*
616 Automatic Dendritic Spine Quantification from Confocal Data with Neurolucida 360. *Curr*
617 *Protoc Neurosci* 2016; **77:** 1 27 21-21 27 21.
618
619 22. Mateus-Pinheiro A, Alves ND, Patricio P, Machado-Santos AR, Loureiro-Campos E, Silva
620 JM *et al.* AP2gamma controls adult hippocampal neurogenesis and modulates cognitive,
621 but not anxiety or depressive-like behavior. *Mol Psychiatry* 2017; **22**(12)**:** 1725-1734.
622
623 23. Yang G, Pan F, Gan WB. Stably maintained dendritic spines are associated with lifelong
624 memories. *Nature* 2009; **462**(7275)**:** 920-924.
625
626 24. Price KA, Varghese M, Sowa A, Yuk F, Brautigam H, Ehrlich ME *et al.* Altered synaptic
627 structure in the hippocampus in a mouse model of Alzheimer's disease with soluble
628 amyloid-beta oligomers and no plaque pathology. *Mol Neurodegener* 2014; **9:** 41.
629
630 25. Rodriguez A, Ehlenberger DB, Dickstein DL, Hof PR, Wearne SL. Automated three-
631 dimensional detection and shape classification of dendritic spines from fluorescence
632 microscopy images. *PLoS One* 2008; **3**(4)**:** e1997.
633
634 26. Bourne J, Harris KM. Do thin spines learn to be mushroom spines that remember? *Curr*
635 *Opin Neurobiol* 2007; **17**(3)**:** 381-386.
636
637 27. Zuo Y, Lin A, Chang P, Gan WB. Development of long-term dendritic spine stability in
638 diverse regions of cerebral cortex. *Neuron* 2005; **46**(2)**:** 181-189.
639

640 28. Anacker C, Hen R. Adult hippocampal neurogenesis and cognitive flexibility - linking
641 memory and mood. *Nat Rev Neurosci* 2017; **18**(6)**:** 335-346.
642
643 29. Jedlicka P, Vlachos A, Schwarzacher SW, Deller T. A role for the spine apparatus in LTP
644 and spatial learning. *Behav Brain Res* 2008; **192**(1)**:** 12-19.
645
646 30. Moser MB, Trommald M, Andersen P. An increase in dendritic spine density on
647 hippocampal CA1 pyramidal cells following spatial learning in adult rats suggests the
648 formation of new synapses. *Proc Natl Acad Sci U S A* 1994; **91**(26)**:** 12673-12675.
649
650 31. Illouz T, Madar R, Louzoun Y, Griffioen KJ, Okun E. Unraveling cognitive traits using the
651 Morris water maze unbiased strategy classification (MUST-C) algorithm. *Brain Behav*
652 *Immun* 2016; **52:** 132-144.
653
654 32. Magnowska M, Gorkiewicz T, Suska A, Wawrzyniak M, Rutkowska-Wlodarczyk I,
655 Kaczmarek L *et al.* Transient ECM protease activity promotes synaptic plasticity. *Sci Rep*
656 2016; **6:** 27757.
657
658 33. Yamada J, Nadanaka S, Kitagawa H, Takeuchi K, Jinno S. Increased Synthesis of
659 Chondroitin Sulfate Proteoglycan Promotes Adult Hippocampal Neurogenesis in
660 Response to Enriched Environment. *J Neurosci* 2018; **38**(39)**:** 8496-8513.
661
662 34. Vegh MJ, Rausell A, Loos M, Heldring CM, Jurkowski W, van Nierop P *et al.* Hippocampal
663 extracellular matrix levels and stochasticity in synaptic protein expression increase with
664 age and are associated with age-dependent cognitive decline. *Mol Cell Proteomics* 2014;
665 **13**(11)**:** 2975-2985.

666

667 35. Miyata S, Nadanaka S, Igarashi M, Kitagawa H. Structural Variation of Chondroitin Sulfate
668 Chains Contributes to the Molecular Heterogeneity of Perineuronal Nets. *Front Integr*
669 *Neurosci* 2018; **12:** 3.

670

671 36. Zimmermann DR, Dours-Zimmermann MT. Extracellular matrix of the central nervous
672 system: from neglect to challenge. *Histochem Cell Biol* 2008; **130**(4)**:** 635-653.

673

674 37. Rowlands D, Lensjo KK, Dinh T, Yang S, Andrews MR, Hafting T *et al.* Aggrecan Directs
675 Extracellular Matrix-Mediated Neuronal Plasticity. *J Neurosci* 2018; **38**(47)**:** 10102-10113.

676

677 38. Fawcett JW, Oohashi T, Pizzorusso T. The roles of perineuronal nets and the perinodal
678 extracellular matrix in neuronal function. *Nat Rev Neurosci* 2019; **20**(8)**:** 451-465.

679

680 39. Gogolla N, Caroni P, Luthi A, Herry C. Perineuronal nets protect fear memories from
681 erasure. *Science* 2009; **325**(5945)**:** 1258-1261.

682

683 40. Romberg C, Yang S, Melani R, Andrews MR, Horner AE, Spillantini MG *et al.* Depletion
684 of perineuronal nets enhances recognition memory and long-term depression in the
685 perirhinal cortex. *J Neurosci* 2013; **33**(16)**:** 7057-7065.

686

687 41. Cope EC, Gould E. Adult Neurogenesis, Glia, and the Extracellular Matrix. *Cell Stem Cell*
688 2019; **24**(5)**:** 690-705.

689

690 42. Dansie LE, Ethell IM. Casting a net on dendritic spines: the extracellular matrix and its
691 receptors. *Dev Neurobiol* 2011; **71**(11)**:** 956-981.

692

693 43. Singhal N, Martin PT. Role of extracellular matrix proteins and their receptors in the
694 development of the vertebrate neuromuscular junction. *Dev Neurobiol* 2011; **71**(11)**:** 982-
695 1005.

696

697 44. Jaworski DM, Perez-Martinez L. Tissue inhibitor of metalloproteinase-2 (TIMP-2)
698 expression is regulated by multiple neural differentiation signals. *J Neurochem* 2006;
699 **98**(1)**:** 234-247.

700

701 45. Wang S, Brunne B, Zhao S, Chai X, Li J, Lau J *et al.* Trajectory Analysis Unveils Reelin's
702 Role in the Directed Migration of Granule Cells in the Dentate Gyrus. *J Neurosci* 2018;
703 **38**(1)**:** 137-148.

704

705 46. Levy AD, Omar MH, Koleske AJ. Extracellular matrix control of dendritic spine and
706 synapse structure and plasticity in adulthood. *Front Neuroanat* 2014; **8:** 116.

707

708 47. Choi YS, Vincent LG, Lee AR, Kretchmer KC, Chirasatitsin S, Dobke MK *et al.* The
709 alignment and fusion assembly of adipose-derived stem cells on mechanically patterned
710 matrices. *Biomaterials* 2012; **33**(29)**:** 6943-6951.

711

712 48. Vincent LG, Choi YS, Alonso-Latorre B, del Alamo JC, Engler AJ. Mesenchymal stem cell
713 durotaxis depends on substrate stiffness gradient strength. *Biotechnol J* 2013; **8**(4)**:** 472-
714 484.

715

716 49. Saha K, Keung AJ, Irwin EF, Li Y, Little L, Schaffer DV *et al.* Substrate modulus directs
717 neural stem cell behavior. *Biophys J* 2008; **95**(9)**:** 4426-4438.

718

719 50. Leipzig ND, Shoichet MS. The effect of substrate stiffness on adult neural stem cell
720 behavior. *Biomaterials* 2009; **30**(36)**:** 6867-6878.
721

722 51. Rammensee S, Kang MS, Georgiou K, Kumar S, Schaffer DV. Dynamics of
723 Mechanosensitive Neural Stem Cell Differentiation. *Stem Cells* 2017; **35**(2)**:** 497-506.
724

725 52. Barnes JM, Przybyla L, Weaver VM. Tissue mechanics regulate brain development,
726 homeostasis and disease. *J Cell Sci* 2017; **130**(1)**:** 71-82.
727

728 53. Hall CM, Moeendarbary E, Sheridan GK. Mechanobiology of the brain in ageing and
729 Alzheimer's disease. *Eur J Neurosci* 2021; **53**(12)**:** 3851-3878.
730

731 54. Javier-Torrent M, Zimmer-Bensch G, Nguyen L. Mechanical Forces Orchestrate Brain
732 Development. *Trends Neurosci* 2021; **44**(2)**:** 110-121.
733

734 55. Keren-Shaul H, Spinrad A, Weiner A, Matcovitch-Natan O, Dvir-Szternfeld R, Ulland TK
735 *et al.* A Unique Microglia Type Associated with Restricting Development of Alzheimer's
736 Disease. *Cell* 2017; **169**(7)**:** 1276-1290 e1217.
737

738 56. Birch HL. Extracellular Matrix and Ageing. *Subcell Biochem* 2018; **90:** 169-190.
739

740 57. Sun Y, Xu S, Jiang M, Liu X, Yang L, Bai Z *et al.* Role of the Extracellular Matrix in
741 Alzheimer's Disease. *Front Aging Neurosci* 2021; **13:** 707466.
742

743 58. Bettio LEB, Rajendran L, Gil-Mohapel J. The effects of aging in the hippocampus and
744 cognitive decline. *Neurosci Biobehav Rev* 2017; **79:** 66-86.
745
746 59. Vegh MJ, Heldring CM, Kamphuis W, Hijazi S, Timmerman AJ, Li KW *et al.* Reducing
747 hippocampal extracellular matrix reverses early memory deficits in a mouse model of
748 Alzheimer's disease. *Acta Neuropathol Commun* 2014; **2:** 76.
749
750 60. Moreno-Jimenez EP, Flor-Garcia M, Terreros-Roncal J, Rabano A, Cafini F, Pallas-
751 Bazarra N *et al.* Adult hippocampal neurogenesis is abundant in neurologically healthy
752 subjects and drops sharply in patients with Alzheimer's disease. *Nat Med* 2019; **25**(4)**:**
753 554-560.
754
755

756 **Figure 1**

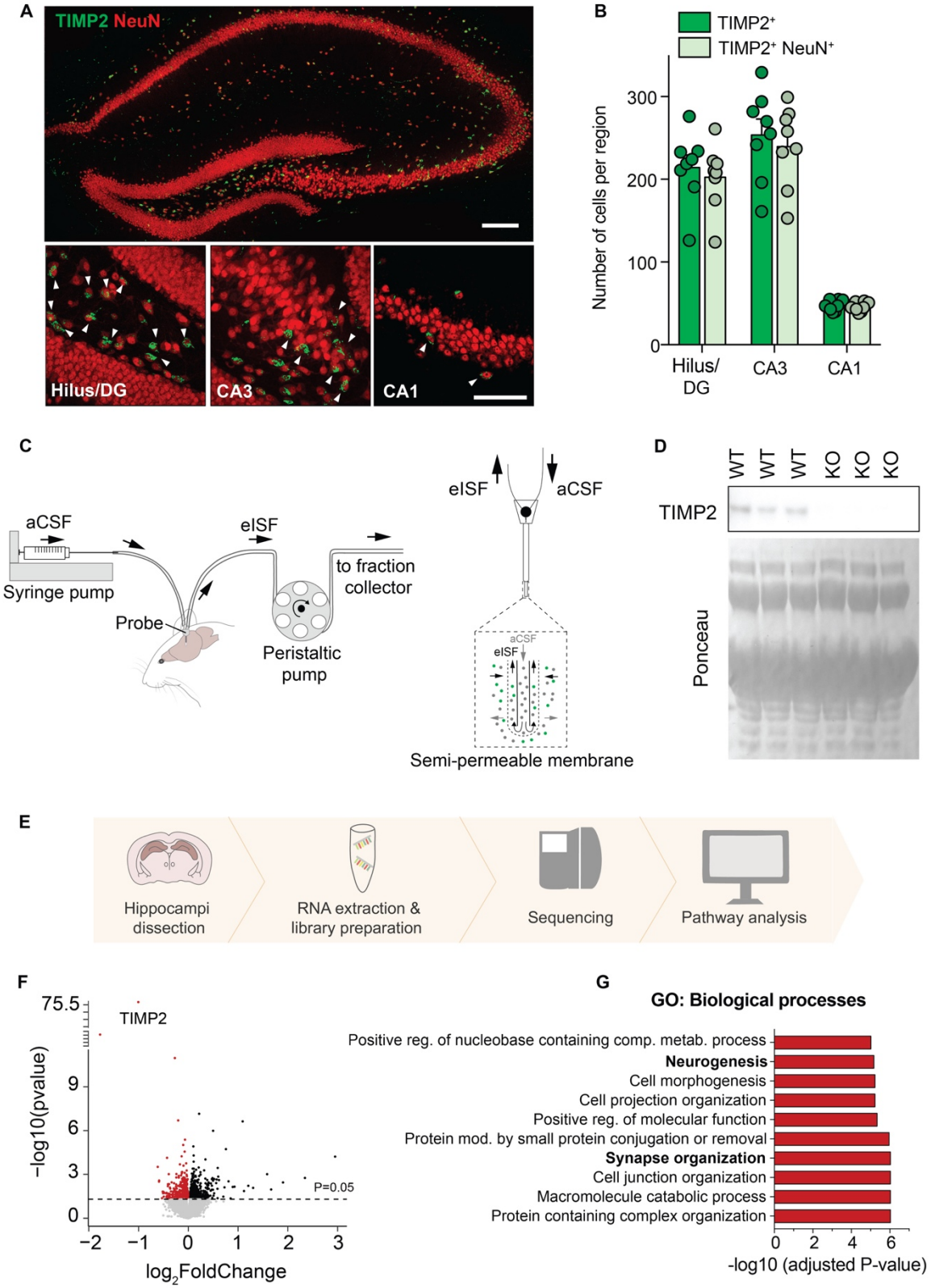
A
TIMP2 NeuN
Hilus/DG
CA3
CA1
B
TIMP2+
TIMP2+ NeuN+
Number of cells per region
300
200
100
0
Hilus/ DG
CA3
CA1
C
aCSF
Syringe pump
eISF
Probe
Peristaltic pump
to fraction collector
eISF
aCSF
aCSF
eISF
Semi-permeable membrane
D
WT
WT
WT
KO
KO
KO
TIMP2
Ponceau
E
Hippocampi dissection
RNA extraction & library preparation
Sequencing
Pathway analysis
F
75.5
TIMP2
−log10(pvalue)
9
6
3
0
P=0.05
−2
−1
0
1
2
3
log2FoldChange
G
GO: Biological processes
Positive reg. of nucleobase containing comp. metab. process
Neurogenesis
Cell morphogenesis
Cell projection organization
Positive reg. of molecular function
Protein mod. by small protein conjugation or removal
Synapse organization
Cell junction organization
Macromolecule catabolic process
Protein containing complex organization
0
2
4
6
-log10 (adjusted P-value)

757 **Figure 1. TIMP2 is expressed in neurons of the hippocampus, and its deletion induces**
758 **transcriptomic changes**. **(A)** Low-magnification view (upper image) of mouse hippocampus and
759 high-magnification view (lower images) of hilus/DG, CA3, and CA1 subregions showing $TIMP2^+$
760 cells and $TIMP2^+$ cells staining for pan-neuronal nuclei marker NeuN. Scale bars, 200 μm and 20
761 μm (inset). **(B)** Quantification of the total number of $TIMP2^+$ cells and $TIMP2^+$ $NeuN^+$ cells across
762 hippocampal subregions in WT mice (2 months of age; N = 8, males and females). **(C)** Schematic
763 representation of high molecular weight cut-off (1-MDa) *in vivo* microdialysis for assessing TIMP2
764 levels in mouse hippocampal ISF. **(D)** TIMP2 immunoblotting of hippocampal ISF dialyzed from
765 2-month-old WT and TIMP2 KO mice, with corresponding Ponceau S stain. **(E)** Schematic
766 representation of bulk RNA-seq workflow performed in isolated WT and TIMP2 KO hippocampi
767 (N = 13-17/group, sex-matched) for transcriptomic analysis. **(F)** Volcano plot showing the fold-
768 change of genes (log_2 scale) differentially expressed in hippocampus of TIMP2 KO vs. WT mice.
769 Downregulated DEGs at $P < 0.05$ are highlighted in red (upregulated in black). **(G)** Top 10
770 significant pathways for downregulated DEGs from Gene Set Enrichment Analysis. Data are
771 represented as mean ± SEM. DG, dentate gyrus; eISF, exchangeable interstitial fluid; aCSF,
772 artificial cerebrospinal fluid.
773

774 **Figure 2**

775

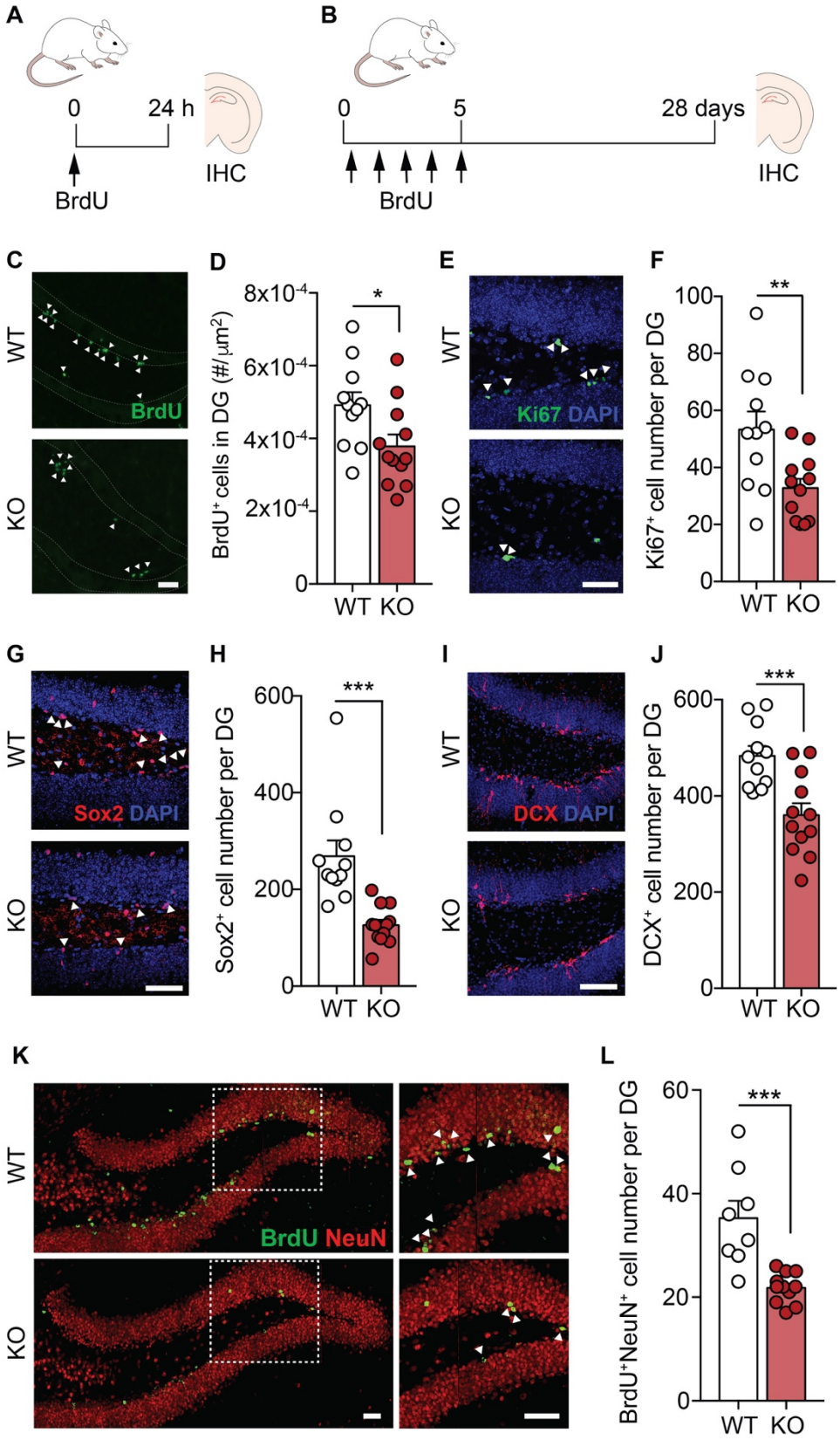

776 **Figure 2. TIMP2 is necessary for adult neurogenesis in the normal dentate gyrus.**
777 **(A)** Schematic timeline of BrdU intraperitoneal injection protocol to label proliferating cells in the
778 DG in isolated brain sections. **(B)** Schematic timeline of BrdU intraperitoneal injection protocol
779 used for cell fate "survival" labeling in DG of isolated brain sections. **(C)** Representative confocal
780 microscopy images of $BrdU^+$ cells in the DG of WT and TIMP2 KO mice (2-3 months of age, N =
781 11-12 mice per group; arrowheads indicate $BrdU^+$ cells; scale bar, 50 μm) with corresponding **(D)**
782 quantification of number of $BrdU^+$ cells in the dentate gyrus per unit area. **(E)** Representative
783 confocal microscopy images of proliferating $Ki67^+$ cells in the DG of WT and TIMP2 KO mice (2-
784 3 months of age, N = 11-12 mice per group; arrowheads indicate $Ki67^+$ cells; scale bar, 50 μm)
785 with corresponding **(F)** quantification of the number of $Ki67^+$ proliferating cells per DG in WT and
786 TIMP2 KO mice. **(G)** Representative confocal microscopy images of $Sox2^+$ in the DG of WT and
787 TIMP2 KO mice (2-3 months of age, N = 11-12 mice per group; arrowheads indicate $Sox2^+$ cells;
788 scale bar, 50 μm) with corresponding **(H)** quantification of $Sox2^+$ neural progenitor cells in the DG
789 of WT and TIMP2 KO mice. **(I)** Representative confocal microscopy images of DCX^+ cells in the
790 DG of WT and TIMP2 KO mice (2-3 months of age, N = 11-12 mice per group; scale bar, 50 μm)
791 with corresponding **(J)** quantification of DCX^+ immature neuroblasts in DG of WT and TIMP2 KO
792 mice. **(K)** Representative confocal microscopy images of $BrdU^+$ $NeuN^+$ cells in DG of WT and
793 TIMP2 KO mice (2-3 months of age. N = 8-11 mice per group; scale bar, 50 μm and 100 μm
794 (inset)) with corresponding **(L)** quantification of newborn neurons ($BrdU^+$ $NeuN^+$ cells) in the DG
795 of WT and TIMP2 KO mice. Data are represented as mean ± SEM. Student's *t*-test for two-group
796 comparisons. *P<0.05; **P<0.01; ***P<0.001. Data points represent individual mice. IHC,
797 immunohistochemistry; DG, dentate gyrus; DCX, doublecortin.
798

799 **Figure 3**
800

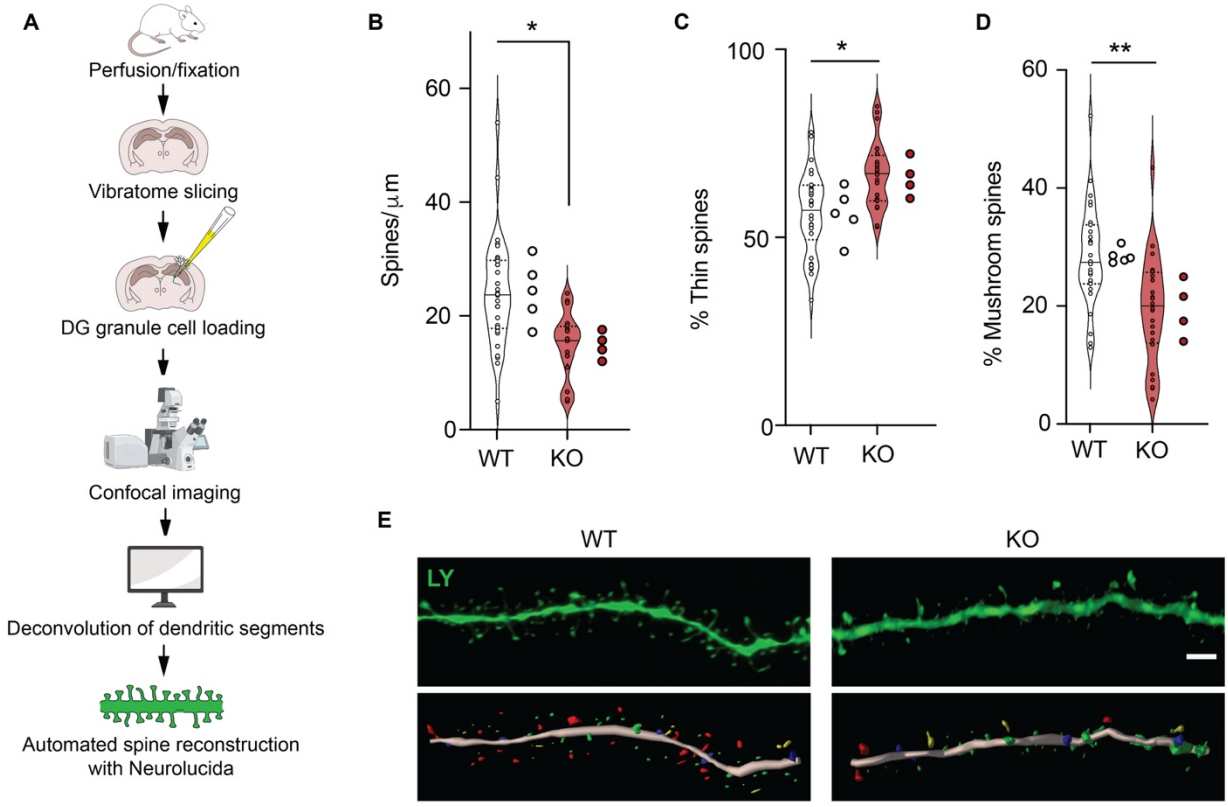

801 **Figure 3. TIMP2 regulates dendritic spine plasticity within the dentate gyrus.**

802 **(A)** Schematic representation of the workflow for dendritic spine quantification in Lucifer Yellow-
803 filled DG granule cells. **(B)** Overall dendritic spine density in DG granule cells iontophoretically
804 labeled with Lucifer Yellow using sections isolated from six-month-old WT and TIMP2 KO mice
805 (N = 6 neurons per mouse from N = 4-5 mice per group). **(C)** Quantification of the percentage of
806 spines categorized according to "thin" spine heads or **(D)** "mushroom" spine heads. **(E)**
807 Representative deconvolved confocal image of a dendritic segment from WT and TIMP2 KO
808 Lucifer Yellow-labeled brain sections, and the downstream 3D reconstructions, with dendritic
809 segment shown in pink, thin spines in green, stubby in blue, mushroom in red, and filopodia in
810 yellow. Scale bar, 2 μm. Data are represented as mean ± SEM. Nested t-test for comparisons
811 with neuron and mouse as levels. *P<0.05; **P<0.01. Data points represent neurons (left) and
812 mice (right) for each group. LY, Lucifer Yellow

813

814 **Figure 4**

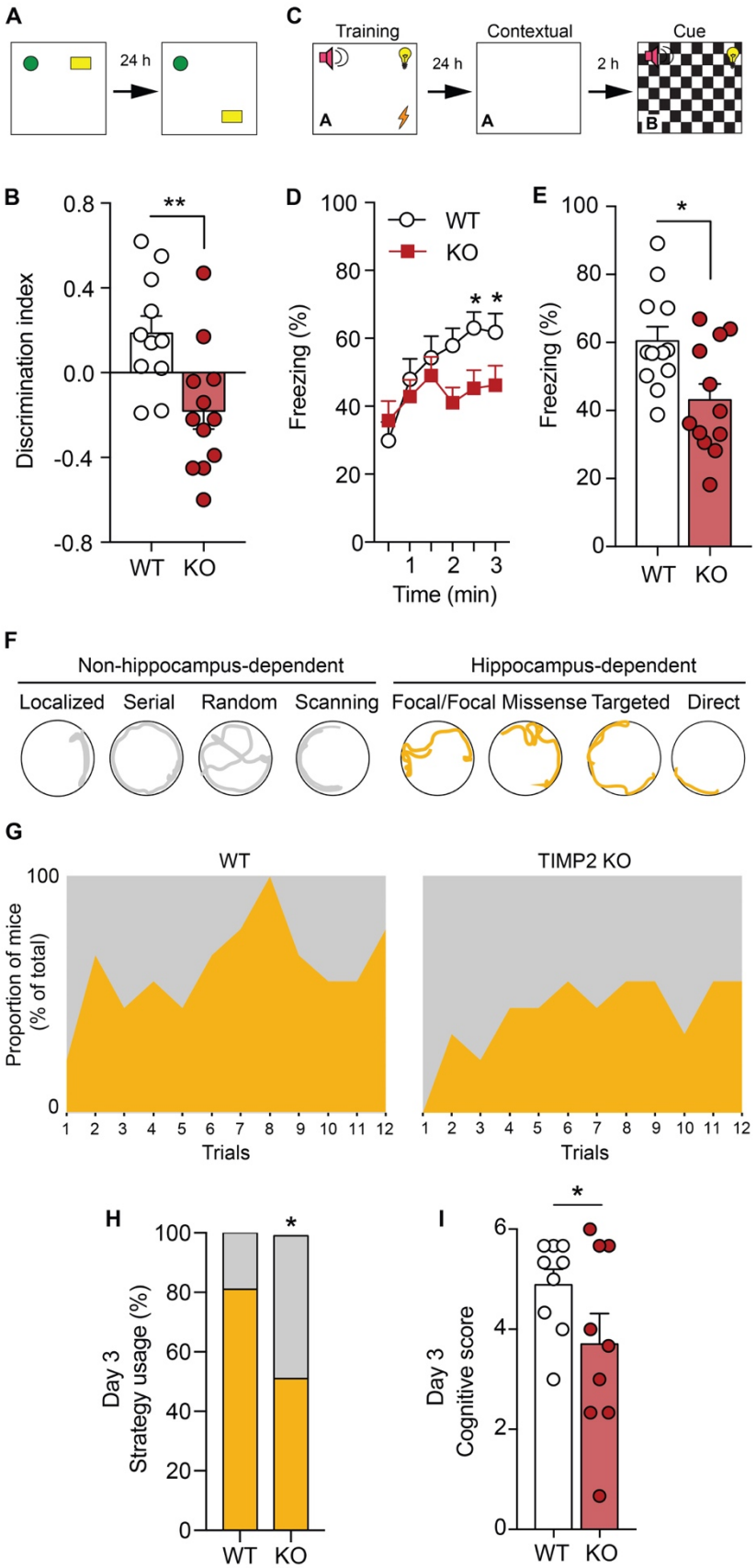
A
24 h
C
Training
Contextual
Cue
24 h
2 h
A
A
B
B
Discrimination index
0.8
0.4
0.0
-0.4
-0.8
**
WT
KO
D
Freezing (%)
100
80
60
40
20
0
WT
KO
* *
1
2
3
Time (min)
E
Freezing (%)
100
80
60
40
20
0
*
WT
KO
F
Non-hippocampus-dependent
Hippocampus-dependent
Localized
Serial
Random
Scanning
Focal/Focal
Missense
Targeted
Direct
G
WT
TIMP2 KO
Proportion of mice
(% of total)
100
0
1 2 3 4 5 6 7 8 9 10 11 12
Trials
1 2 3 4 5 6 7 8 9 10 11 12
Trials
H
Day 3
Strategy usage (%)
100
80
60
40
20
0
*
WT
KO
I
Day 3
Cognitive score
6
4
2
0
*
WT
KO

815 **Figure 4. TIMP2 is required for hippocampus-dependent memory function.**

816 **(A)** Schematic of the novel location recognition assay. **(B)** Discrimination index for novel location
817 recognition on day 2 for WT and TIMP2 KO mice (2-3 months of age, N = 11-12 mice per group).
818 **(C)** Schematic of the contextual and cued fear-conditioning assay. **(D, E)** Freezing levels by
819 interval and overall measured in the conditioned-fear context A in WT and TIMP2 KO mice (2-3
820 months of age, N = 11-12 mice per group). **(F)** Schematic diagram of modified Barnes maze with
821 color coding for overall strategy classification. **(G)** Proportion of WT and TIMP2 KO mice using
822 non-hippocampus-dependent (gray) and hippocampus-dependent (yellow) strategies during the
823 testing trials (2-3 months of age, N = 9 mice per group). **(H)** Strategy utilization by WT and TIMP2
824 KO mice on day 3 of the Barnes Maze and corresponding **(I)** cognitive scores, ranked by strategy
825 complexity for WT and TIMP2 KO mice on day 3 in the Barnes Maze. Data are represented as
826 mean ± SEM. Student's t-test for two-group comparisons in **(B, D, E)**, chi-square test in **(H)**, and
827 nested t-test **(I)** for trial and mouse levels. *P<0.05, **P<0.01. Data points represent individual
828 mice.

829

830

831 **Figure 5**
832

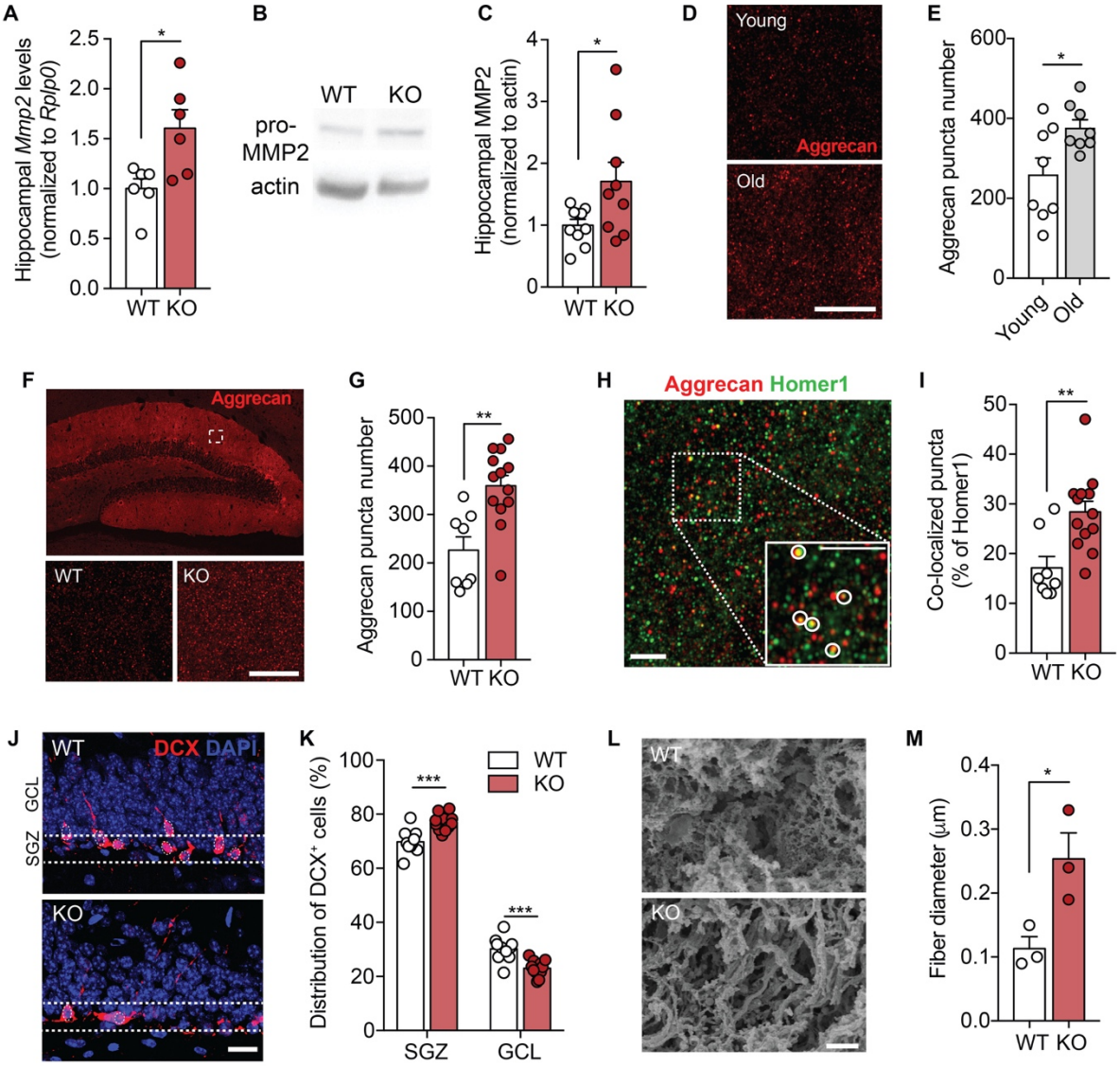

833 **Figure 5. TIMP2 ablation leads to accumulation of ECM within the hippocampus.**

834 **(A)** *Mmp2* mRNA levels by qPCR from isolated hippocampus of WT and TIMP2 KO mice (2-3
835 months of age, N = 6 mice per group). **(B)** Immunoblotting of MMP2 from hippocampal lysates of
836 WT and TIMP2 KO mice (2-3 months of age, N = 9 mice per group) with corresponding **(C)**
837 quantification of MMP2 protein levels. **(D)** Representative confocal microscopy images of
838 aggrecan puncta in the molecular layer of the DG from young (3-month-old) and old (21-month-
839 old) mice (N = 8 mice per group; scale bar, 5 μm), with corresponding **(E)** quantification of
840 aggrecan puncta number. **(F)** Representative confocal microscopy images showing aggrecan
841 puncta in the molecular layer of DG at low-magnification (top) and high-magnification (bottom) of
842 analysis inset from WT and TIMP2 KO mice (2-3 months of age, N = 8-13 mice per group; scale
843 bar, 5 μm) with corresponding **(G)** quantification of puncta. **(H)** Representative confocal
844 microscopy image indicating colocalized puncta (see inset) with corresponding **(I)** quantification
845 of aggrecan and homer1 co-localization in the molecular layer of DG from WT and TIMP2 KO
846 mice (2-3 months of age, N = 8-13 mice per group; scale bar, 2.5 μm). **(J)** Representative images
847 showing the migration of DCX^+ cells in the SGZ and GCL of WT and TIMP2 KO mice (2-3 months
848 of age, N = 11-12 mice per group, scale bar, 20 μm with corresponding **(K)** quantification of DCX^+
849 cells distributed in the subgranular zone (SGZ) and granule cell layer (GCL) of DG. **(L)**
850 Representative surface scanning electron microscopy (SEM) from DG of WT and TIMP2 KO mice
851 (2-3 months of age, N = 3 mice per group, scale bar, 2 μm, with corresponding **(M)** quantification
852 of ECM microarchitecture in terms of fiber diameter measurements. Data are represented as
853 mean ± SEM. Student's t-test for two-group comparisons. *P<0.05, ** P<0.01, ***P<0.001. Data
854 points represent individual mice.

855

856

857 **Figure 6**
858

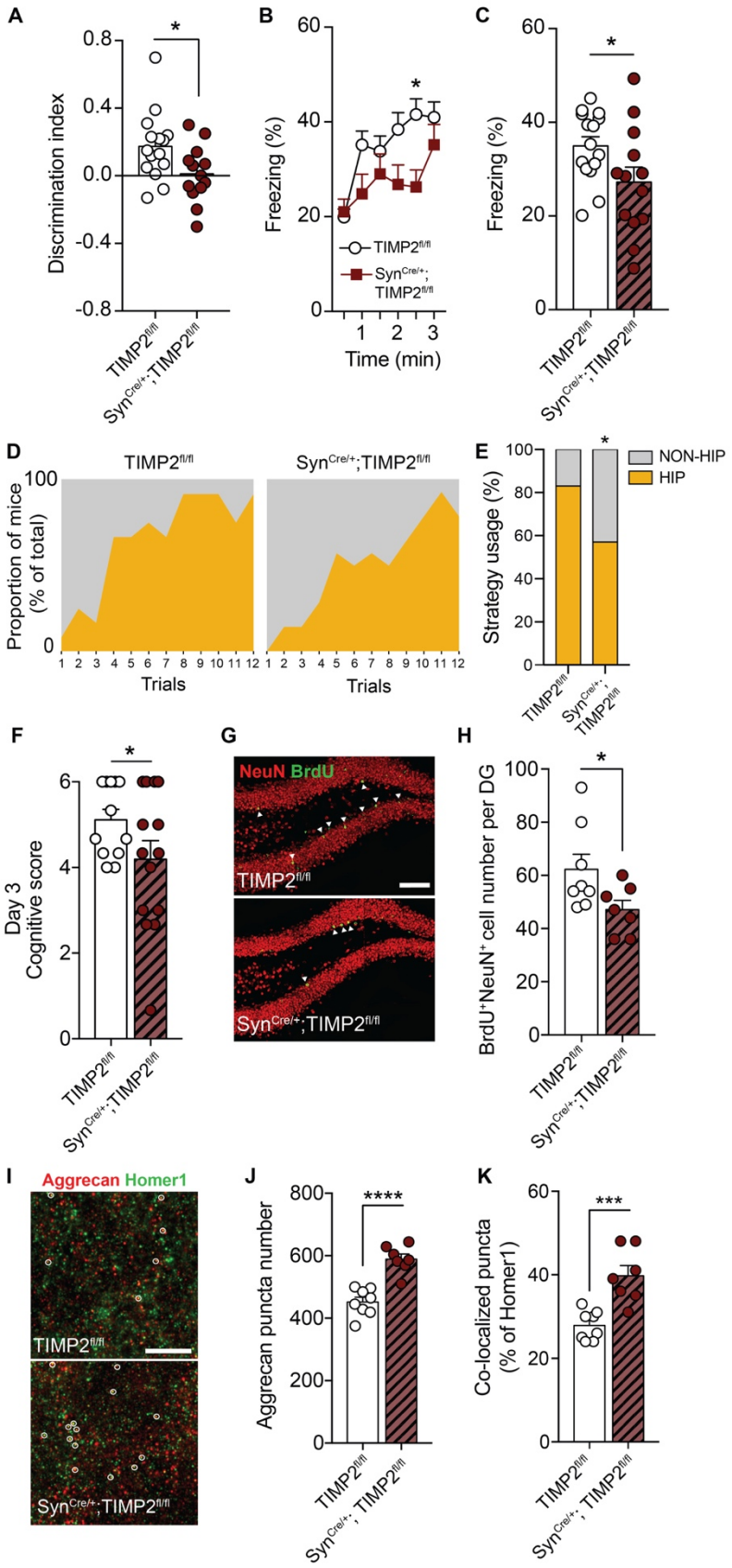

859 **Figure 6. Neuronal TIMP2 regulation of the extracellular matrix regulates hippocampus-**
860 **dependent cognitive function and adult neurogenesis.**
861 **(A)** Discrimination index for novel location recognition on day 2 and **(B, C)** contextual fear-
862 conditioning freezing levels in $TIMP2^{fl/fl}$ and $Syn^{Cre/+}$; $TIMP2^{fl/fl}$ mice (2-3 months of age, N = 13-
863 15 mice per group). **(D)** Proportion of mice of each genotype using non-hippocampus-dependent
864 (gray) and hippocampus-dependent (yellow) search strategies during the testing trials of $TIMP2^{fl/fl}$
865 and $Syn^{Cre/+}$; $TIMP2^{fl/fl}$ mice in Barnes maze (2-3 months of age, N = 12-14 mice per group) with
866 **(E)** quantification of the percentage of mice using these strategies by on day 3. **(F)** Cognitive
867 complexity scores for $TIMP2^{fl/fl}$ and $Syn^{Cre/+}$; $TIMP2^{fl/fl}$ mice based on strategies used on day 3 of
868 Barnes maze. **(G)** Representative confocal microscopy images of $BrdU^+$ and $NeuN^+$ cells in DG
869 of $TIMP2^{fl/fl}$ and $Syn^{Cre/+}$; $TIMP2^{fl/fl}$ mice (2-3 months of age, N = 7–8 mice per group, scale bar,
870 100 μm) with corresponding **(H)** quantification of $BrdU^+$ $NeuN^+$ newborn neurons in the DG. **(I)**
871 Representative confocal microscopy images of aggrecan and homer1 puncta in molecular layer
872 of DG of $TIMP2^{fl/fl}$ and $Syn^{Cre/+}$; $TIMP2^{fl/fl}$ mice (N = 7-8 mice per group, scale bar, 5 μm) with
873 corresponding **(J)** quantification of aggrecan puncta and **(K)** co-localized puncta of aggrecan and
874 homer1, as indicated by overlaid circles. Data are represented as mean ± SEM. Student's *t*-test
875 for two-group comparisons in **(A-C)**, **(H)**, and **(J, K)**, chi-square test in **(E)**, and nested t-test **(F)**
876 with trial and mice as levels. *P<0.05, ** P<0.01, ***P<0.001, ****P<0.0001. Data points represent
877 individual mice.
878

879 **Supplementary Information, *Materials and Methods and Supplementary Figures***

880

881 **Supplementary Materials and methods**

882

883 **Generation of TIMP2-floxed mice**

884 To achieve conditional deletion of *Timp2*, a loxP-flanked *Timp2* allele (TIMP2$^{fl/fl}$) was generated
885 by the two-cell homologous recombination (2C-HR)-CRISPR/Cas9-based genome editing
886 method, as previously described[1]. Briefly, two loxP sites were inserted into the *Timp2* gene
887 flanking exon 2, with homologous arms (HA) on each side. Two point-mutations (C928->A near
888 the end of the left arm and G1795->T at the 5' junction of the right arm) were introduced to disrupt
889 the PAM sequence to avoid re-cutting of the recombined allele. Three nucleotides adjacent to
890 each loxP site were altered to create restriction sites for diagnostic purposes: XbaI near the
891 upstream loxP, and HindIII near the downstream loxP site. The two-cell stage embryo
892 microinjection procedure was performed as in[1], using Cas9-mSA mRNA, biotinylated double-
893 stranded PCR product (1016 nts), and pre-assembled ctRNA prepared accordingly[1]. F_0 mice were
894 screened by sequencing from TOPO cloned PCR product, using tail genomic DNA, amplified from
895 the TIMP2 target region, and using the following primers: FW-AGCGACCGATAAGCAGGAAG,
896 Rev-CACTAGCAGACACCACCACA. Identified founders were crossed with wild-type (WT)
897 C57BL/6J mice, purchased from The Jackson Laboratory, to produce heterozygous mice.

898 To achieve neuron-specific *Timp2* deletion, neuron-specific heterozygous Synapsin (Syn)-
899 Cre (Syn$^{Cre/+}$) transgenic mice[2] (JAX stock #003966) were crossbred with TIMP2$^{fl/fl}$ mice to
900 generate Syn$^{Cre/+}$; TIMP2$^{fl/+}$ progeny. The F_1 mice were then crossed to generate Syn$^{Cre/+}$; TIMP2$^{fl/fl}$
901 and TIMP2$^{fl/fl}$ littermate controls. Cre expression was maintained in the female mice for breeding[2].
902 All animals were maintained on a C57Bl/6J background.

903

904 **Genotyping**

905 Genotyping of TIMP2$^{fl/fl}$ mice was performed using the following primers: *Primer 1*: 5'-
906 TGACCCCTCTGCTCTAGTCC, *Primer 2:* 5'-GCTCCGTCTCTTCGTCCATC (**Figure 6A**).
907 Genomic DNA was extracted from the tail using the QIAamp Fast DNA Tissue Kit (Qiagen). PCR
908 was performed in a total volume of 50 µl at 94°C for 2 min, 94°C for 30 s, 61°C for 30 s, 68°C for
909 2 min and 15 sec for 10 cycles, then 94°C for 30 s, 56°C for 30 s, 68°C for 2 min and 15 s for 25
910 cycles, and ending at 72°C for 5 min using Prime STAR (#R050A, TaKaRa, Shiga, Japan). For
911 loxP site verification based on restriction digest, the PCR product (2.1 kb) was digested with XbaI
912 and HindIII restriction enzymes (New England Biolabs, Ipswich, MA, USA) at 37°C for 1 hour,
913 followed by 10 min at 65°C for heat inactivation. Digested PCR products were run on an agarose
914 gel and imaged for the identification of founders: HindIII (WT: 2133 bp; upstream loxP positive:
915 829 bp and 1,304 bp); Xba1 (WT: 2133 bp; downstream loxP positive: 566 bp and 1,567 bp).
916
917 **In vivo microdialysis**
918 For guide cannula implantation into the hippocampus, mice were anesthetized with 2% isoflurane
919 and head was shaved prior to being fixed in a stereotaxic apparatus (Stoelting Co., Wood Dale,
920 IL, USA). After preparing skin with 70% ethanol and povidone-iodine, an anterior-to-posterior
921 incision was made along the midline of the head to expose the skull. Skull position was leveled to
922 within 0.1 mm along the bregma-lambda axis, and at 2.2 mm to the left and right of midline on the
923 lateral axis. Holes were drilled to target the left hippocampus using the stereotaxic coordinates:
924 bregma -3.1 mm, 2.5 mm lateral. A second hole was made diagonally to the first, to serve as an
925 anchoring position with a bone screw. To target caudal hippocampus, AtomosLM Guide Cannula
926 (PEG-12, Eicom, London, UK) was inserted at a 12° angle, 1.2 mm below the dura mater. Dental
927 cement was applied to secure the cannula, and the skin was secured using a surgical adhesive
928 glue. An AtmosLM Dummy Cannula (PED-12, Eicom) was inserted into the guide cannula and
929 secured with a plastic cap nut. Animals were then placed in a clean cage on a heating pad and
930 allowed to recover from surgery.

931 Approximately 12 hours following surgery, mice underwent 1000-kDa *in vivo* microdialysis.
932 The inlet port of AtmosLM Microdialysis Probe (PEP-12-02, Emicon) was connected to a syringe
933 pump (kdScientific, Holliston, MA, USA) perfusing artificial cerebrospinal fluid (aCSF), in mM: 1.3
934 $CaCl_2$, 1.2 $MgSO_4$, 3 KCl, 0.4 KH_2PO_4, 25 $NaHCO_3$, 122 NaCl, pH 7.35, at a rate of 1.2 µl/min[3].
935 The outlet of the probe was connected to the peristaltic pump (MAB 20, SciPro, New York, NY,
936 USA), which was calibrated to obtain a pull rate between 1-1.1 µl/min. After the probe was
937 connected to the push-pull mechanism, the mice were briefly anesthetized with isoflurane to allow
938 for the removal of the dummy cannula and insertion of the probe into the hippocampus. The probe
939 was secured with a cap nut, and a plastic collar was loosely placed around the neck of the mouse.
940 Mice were then moved to a Raturn (Stand-Alone Raturn System, BASi,
941 West Lafayette, IN, USA) and tethered by the collar to avoid tangling microdialysis tubing (FEP
942 tubing 0.65 mm OD x 0.12 mm ID, BASi), while allowing for free movement of the mouse during
943 the sample collection period. Samples were collected hourly in a refrigerated fraction collector
944 (MAB 85 Fraction Collector, SciPro) and frozen at −80°C after collection. The procedure was
945 performed under constant light conditions, and food and water were provided *ad libitum*.
946
947 **Bulk RNA-sequencing**
948 RNA-sequencing was performed on hippocampi dissected from WT and TIMP2 KO male and
949 female mice. Dissected hippocampi were preserved in RNAlater (Invitrogen) overnight at 4°C
950 before storing at −80°C until use. RNA was extracted using the RNeasy Mini Kit (Qiagen),
951 according to the manufacturer's instructions. RNA quality was measured using the Agilent
952 TapeStation Bioanalyzer (Agilent Technologies), and all samples exhibited RNA Integrity Number
953 (RIN) > 8. cDNA libraries were prepared with poly(A) selection and sequenced using Illumina
954 Hiseq (2x150bp paired-end) (Genewiz). At least 25 M clean reads were generated from each
955 sample. The reads were mapped to the *Mus musculus* GRCm38 reference genome available on
956 ENSEMBL, using STAR aligner (v.2.5.2b). After extraction of gene hit counts, the gene hit counts

957 table was used for downstream differential expression analysis, using DESeq2 software. The
958 Wald test was used to generate *P*-values and log2 fold changes. Differentially expressed genes
959 (DEGs; $P<0.05$) were used for Gene Set Enrichment Analysis (GSEA; https://www.gsea-
960 msigdb.org/gsea/index.jsp). Volcano plot was generated with R v4.1.2.
961

962 **Immunohistochemistry and microscopy**

963 For all immunohistochemistry experiments, mice were anesthetized with a cocktail of ketamine
964 (90 mg/kg) and xylazine (10 mg/kg) and transcardially perfused with ice-cold 0.9% saline. Brains
965 were dissected, and hemibrains isolated for immunohistochemistry were postfixed in 4%
966 paraformaldehyde (PFA) for 48 hours at 4°C before preservation in 30% sucrose (Sigma, St.
967 Louis, MO, USA) solution in phosphate-buffered saline (PBS). Hemibrains were sectioned
968 coronally at 40-μm thickness on a freezing-sliding microtome (SM2010R, Leica, Deer Park, IL,
969 USA), and sections were stored in cryoprotective medium at −20°C.

970 For immunohistochemistry, free-floating brain sections were permeabilized with Tris-
971 buffer saline (TBS) plus 0.05% Tween-20 (TBST) and incubated in a blocking solution consisting
972 of 10% normal goat (#S-1000, Vector Laboratories, Newark, CA, USA) or donkey serum (#017-
973 000-121, Jackson ImmunoResearch, West Grove, PA, USA) in TBST. Sections were then
974 incubated with primary antibodies in 2% goat or donkey serum in TBST overnight at 4°C. Sections
975 were incubated with primary antibodies, including the following: TIMP2 (1:100; #AF971, R&D
976 Systems, Minneapolis, MN, USA), NeuN (1:200; #MAB377, Millipore, Burlington, MA, USA),
977 doublecortin (DCX; 1:200; #4604S, Cell Signaling, Danvers, MA, USA), Sox2 (1:200; #sc365823,
978 Santa Cruz, Dallas, TX, USA), Ki67 (1:200; #14-5698-82, Thermo Fisher, Waltham, MA, USA),
979 aggrecan (1:500; #AB1031, Millipore), Homer1 (1:500; #160006, Synaptic Systems, Göttingen,
980 Germany). The next day, sections were washed in TBST three times for 5 min each and incubated
981 with Alexa Fluor-conjugated secondary antibodies at 1:200 in TBST for 1 hour at RT. Secondary
982 antibodies used were: Alexa Fluor 594-labeled donkey anti-rabbit (#A-21206), Alexa Fluor 594-

983 labeled donkey anti-mouse (#A-21203), Alexa Fluor 488-donkey anti-rat (#A-21208), Alexa Fluor
984 488-donkey anti-goat (#A-11055), Alexa Fluor 647-donkey anti-mouse (#A-31571), Alexa Fluor
985 594-goat anti-rabbit (#A-11012), Alexa Fluor 5488-goat anti-chicken (#A-11039), all from Thermo
986 Fisher. Brain sections were then washed, stained with 4′,6-diamidino-2-phenylindole (DAPI,
987 Sigma) for 15 min to visualize nuclei, mounted and coverslipped using Prolong Gold (Life
988 Technologies) and dried overnight before imaging. For BrdU staining, brain sections were pre-
989 treated with 3M HCl (Thermo Fisher) for 30 min at 37°C before overnight incubation with primary
990 antibody anti-BrdU (1:500; #ab6326, Abcam, Cambridge, UK) at 4°C. Secondary staining and
991 mounting were performed as described above.
992 Image processing was performed using an LSM 780 confocal microscope (Zeiss, Jena,
993 Germany) using 40x/1.4 Oil DIC objective. Four equally-spaced sections per mouse (rostral
994 through the caudal extent of the DG) were used to count the total number of positive cells within
995 the DG (subgranular zone and hilar subregions) of the hippocampus according to stereological
996 principles. All counts were performed using FIJI in a blinded fashion, according to similar
997 methods[4].
998
999 **Aggrecan and Homer1 puncta quantification**
1000 Quantification of the number of puncta by super-resolution microscopy proceeded similar to the
1001 method described previously[5]. Briefly, images were acquired by confocal microscopy imaging
1002 using an LSM 880 with AiryScan in super-resolution mode (Zeiss) set with a 63X/1.4 Oil DIC
1003 objective with 5X optical zoom. Using consistent laser strength, gain, and digital offset settings
1004 across all sections/experiments, Z stacks were acquired with steps less than the optical slices
1005 acquired. Using Zen software (Zeiss), a setting of 6 ("optimal") was used during AiryScan
1006 processing. Aggrecan puncta were quantified using the Puncta Analyzer plugin[6] in ImageJ, and
1007 thresholding was applied equally across images. For colocalization of co-stained Aggrecan and
1008 Homer1 puncta, images were analyzed with the Puncta Analyzer plugin with a minimum pixel

1009 specification of 4. Three images in the molecular layer of the DG were averaged per mouse for
1010 analysis.
1011
1012 **Dendritic spine analysis by iontophoretic dye injections**
1013 *Tissue processing.* Mice were anesthetized using 15% chloral hydrate and transcardially perfused
1014 with 1% PFA in phosphate buffer (PB, pH 7.4) for 2 min, followed by 4% PFA with 0.125%
1015 glutaraldehyde in PB for 10 min at a rate of 5 ml/min. Brains were dissected and postfixed
1016 overnight at 4°C in the same fixative, and then transferred to PBS with 0.1% sodium azide at 4°C
1017 until sectioned. Brains were hemisected, and the right hemisphere was cut into 200 μm-thick
1018 sections using a vibratome (VT1000S, Leica).
1019
1020 *Intracellular dye injection and confocal imaging*. Coronal sections were incubated in 250 ng/ml
1021 DAPI for 5 min to enable identification of the DG. Sections were mounted on nitrocellulose
1022 membrane filters, immersed in ice-cold PB, and DG granule cells were iontophoretically injected
1023 with 5% Lucifer Yellow (Invitrogen, Waltham, MA, USA) in distilled water under a direct current of
1024 3-8 nA until the dye filled the distal ends of the dendrites. Six to eleven neurons were injected per
1025 section and neurons selected for injection were spaced to avoid overlapping of dendrites.
1026 Sections were mounted with Fluoromount-G (#0100-01, Southern Biotech, Birmingham, AL, USA)
1027 between spacers placed on gelatin-coated glass slides (#22-214-320, Thermo Fisher).
1028 To select dendritic segments for imaging on a Zeiss LSM 780 confocal microscope (Zeiss),
1029 whole cells at the suprapyramidal blade of the DG were first imaged using a 20x/0.8 M27 Plan-
1030 Apochromat objective, using an Ar/Kr laser at an excitation wavelength of 488 nm. Confocal
1031 stacks were acquired at 512 x 512-pixel resolution with a Z-step of 1 μm, a pinhole setting of 1
1032 Airy Unit, and optimal settings for gain and offset. Basal dendritic segments at 50 μm from the
1033 soma were selected for high-resolution imaging according to the following criteria: not a primary
1034 dendrite, no overlap with other dendrites or branching that would obscure spines, not too deep in

1035 the section, and parallel or at acute angles to the coronal plane. Dendritic segments were imaged
1036 using a 100x/1.46 Oil DIC M27 Plan-Apochromat objective, and stacks were acquired at
1037 512 x 512-pixel resolution with a Z-step of 0.1 µm, optical zoom of 3.3x, a pinhole setting of 1 Airy
1038 Unit, and optimal settings for gain and offset. The stacks were imaged with approximately 1 µm
1039 above and below the segment to fully include all spines. Three z-stacks were imaged from each
1040 neuron. Confocal stacks were deconvolved using an iterative blind deconvolution algorithm
1041 (AutoQuant X, vX3.0.1, MediaCybernetics, Rockville, MD, USA).
1042
1043 *Spine reconstruction and analysis.* Deconvolved stacks were analyzed using Neurolucida 360
1044 (v2019.2.1; MBF Bioscience, Williston, VT, USA) for semi-automated reconstruction of dendrites
1045 and spines to determine spine density and morphology. Spines were classified as stubby, thin,
1046 mushroom, and filopodia, based on their morphologies, according to previous work[7]. 4-5 mice per
1047 genotype, 6 neurons per mouse, and 3 dendrites per neuron were analyzed, and violin plots were
1048 used to better visualize the distribution of individual data points.
1049
1050 **Scanning electron microscopy (SEM)**
1051 Following ketamine/xylazine anesthesia and transcardial perfusion with PBS, 2-mm thick brain
1052 slices containing the hippocampus were decellularized, following previously described methods[8].
1053 SEM methods were adapted from a previous study[9]. Decellularized brain slices were fixed in 4%
1054 PFA with 2% glutaraldehyde in 0.1M sodium cacodylate buffer (pH 7.4) for 24 hours at 4°C.
1055 Samples were then briefly rinsed in the same buffer before post-staining with 1% OsO4 for 1 hour.
1056 OsO_4-treated samples were rinsed in water and gradually dehydrated in increasing
1057 concentrations of ethanol (50, 70, 90 100, and 100%, 10 min each). Samples were then stacked
1058 horizontally onto wire mesh dividers to keep them flattened and critical point-dried with liquid CO_2.
1059 Dried samples were mounted onto Aluminum SEM stubs using conductive copper tape and
1060 sputter-coated before imaging with a Zeiss Supra 55 VP FESEM using InLens SE detection at 5

1061 kV operating voltage (Zeiss Microscopy Inc). Fiber diameters were analyzed using Image J
1062 (Bethesda, USA).

1063

1064 **Behavior**

1065 All behavioral analyses were performed during the 0700–1900 light cycle. For all behavioral
1066 experiments, age- (2-3-month-old) and sex-matched mice with corresponding littermate control
1067 animals were used.

1068

1069 *Novel location recognition.* Hippocampus-dependent memory was assessed using the novel
1070 location recognition as previously described[4]. On day 1, the training day, mice were habituated to
1071 the open-field arena for 6 min, an arena that contained wall-mounted visual cues. Mice were
1072 exposed to three consecutive trials of 6 min each, during which they explored two different objects
1073 in fixed positions. On day 2, the testing day, mice explored the same arena as on the training day
1074 but with one object displaced to a novel position. Time spent exploring each object was manually
1075 scored in a blinded fashion to assess the discrimination index for the novel location as the
1076 displaced object interaction time/total interaction time of both objects.

1077

1078 *Contextual fear-conditioning.* Fear-conditioning experiments were performed as previously
1079 described[4] to assess hippocampus-dependent memory. Briefly, mice were trained to associate
1080 the cage context with an aversive stimulus (light foot-shock; Ugo Basile). On the first day, training
1081 parameters included two periods of 30 s consisting of a paired cue light and a tone of 1,000-Hz,
1082 followed by a light foot-shock (2 s, 0.5 mA) separated by a 180-s interval. Chambers were cleaned
1083 with 70% ethanol between experiments by the experimenter. Twenty-four hours later, mice were
1084 re-exposed to the same context for 3 min, and freezing levels (contextual) were measured. Two
1085 hours later, for the cued task, mice were placed in a novel context and exposed to the same tone

1086 and cue light from day 1 (training) after 120 s of exploration. Freezing levels were analyzed for
1087 pre- and post-cue phases. Freezing levels were measured using EthoVision XT system software
1088 (v14.0.1319, Noldus).
1089
1090 *Barnes maze.* Barnes maze testing was performed similarly to that previously described[4]. A large
1091 circular maze containing 40 holes was centered over a pedestal and elevated approximately 40
1092 cm above the floor with a video recording device mounted directly above. The escape hole
1093 consisted of a PVC box similar in texture and color to the surface of the maze. Distinct visual cues
1094 were placed at four equally spaced points around the maze to serve as spatial navigation cues
1095 as the mice navigate the task. The task proceeded over 4 days, with four trials on each day for
1096 each mouse. With overhead illumination and a persistent 2 kHz tone, mice were given 90 s for
1097 each trial to identify the escape hole by jumping in or identifying the hole with extended/overhead
1098 pokes. If mice failed to find the escape hole within 90 s, they were gently guided by light
1099 tapping/directing towards the escape hole and scored with 90 s. The escape hole position was
1100 fixed within a day but changed for each successive day of testing. For each trial within a day, the
1101 starting location for the mouse was rotated relative to the escape hole position. Data collection
1102 and analyses were performed using EthoVision video-tracking system.
1103 Search strategy classification was manually performed and based on methods adapted
1104 from previous work[10], with data collected by EthoVision video-tracking system software. Search
1105 strategies were coded according to the following: (i) localized - minimal movement from the
1106 starting position; (ii) serial - sequential nose points within the outer ring area; (iii) random -
1107 unorganized searching; (iv) scanning - arc-like trajectory, without nose points; (v) focal - direct
1108 search within a maze quadrant; (vi) focal missense - direct search within a maze quadrant from
1109 previous trials; (vii) targeted - direct movement to hole with deviations in the trajectory direction;
1110 (viii) direct - no shifts in the trajectory direction with single nose point to target hole. For strategy
1111 analysis, each related strategy was categorized into non-hippocampus-dependent strategies

1112 comprising localized, serial, random, and scanning strategies, and hippocampus-dependent
1113 strategies that included focal, focal missense, targeted and direct strategies. Cognitive
1114 performance of each trial on day 3 was scored such that cognitive strategies received higher
1115 scores according to the following scale, accounting for high cognitive complexity, with a
1116 separation of 1 point between non-hippocampus-dependent and hippocampus-dependent
1117 strategies: localized = 0, serial = 1, random = 2, scanning = 3, focal = 5, focal missense = 5,
1118 targeted = 6, direct = 6. Focal and focal missense strategies are assigned a score of 5, as both
1119 are goal-directed strategies used without achieving the final target. Target and direct strategies
1120 were assigned score of 6 since both are goal-directed strategies with successful achievement of
1121 the final target.
1122
1123 *Open field*. The open field test was used to evaluate locomotion and exploratory behavior, and
1124 anxiety-like behavior in the center of the arena. The apparatus consisted of a brightly illuminated
1125 square arena of 50 x 50 cm enclosed by walls 45 cm high. Mice were placed individually in the
1126 center of the open field arena, and their movement was traced for 6 min. The resulting data was
1127 analyzed using EthoVision software, considering two previously defined areas: a central and an
1128 outer area. Due to the thigmotaxic exploratory activity of rodents, the ratio between the time spent
1129 in the center and in the periphery of the open field arena can reflect anxiety-like behaviors.
1130 Distance traveled, average velocity, and time spent in each of the zones were recorded and
1131 analyzed.
1132
1133 *Rotarod*. Balance and motor function was measured using the fixed and standard accelerated
1134 rotarod test (Med Associates). The protocol consisted of a first day of training at a constant speed
1135 (4 rpm) for a maximum of 2 min in three trials, with a 2-min interval between each trial. On day 2,
1136 animals were tested for each of 3 different fixed speeds over a range of 4 to 40 rpm for a maximum
1137 of 60 sec each in three trials, with a 2-min interval between each trial. For the acceleration test,

1138 animals were placed on the rod rotating at a constant speed (4 rpm), then the rod started to
1139 accelerate continuously from 4 to 40 rpm over 5 min, in three trials with a 5-min interval between
1140 each trial. The latency to fall off the rotarod was recorded for each trial, and data from three trials
1141 were averaged for each mouse.
1142
1143 *Wire grip test.* Motor coordination and strength was measured by the wire grip task. Each mouse
1144 was placed on a wire cage top, which was slowly inverted and suspended at approximately 30
1145 cm above a mouse cage. The latency of time until the mouse fell off the wire was recorded in
1146 three trials. Mice that did not fall within the 60-s trial period were removed and assigned a maximal
1147 time of 60 s. Data from three trials were averaged for each mouse.
1148
1149 *Clasping.* Mice were suspended by their tail, and the extent of hindlimb clasping was observed
1150 for 15 s. Clasping scoring was based on a previously described method[11]. Briefly, if both hindlimbs
1151 were splayed outward away from the abdomen with splayed toes, a score of 0 was given. If one
1152 hindlimb was retracted or both hindlimbs were partially retracted toward the abdomen without
1153 touching it, and the toes were splayed, a score of 1 was assigned. If both hindlimbs were partially
1154 retracted toward the abdomen and were touching the abdomen without touching each other, a
1155 score of 2 was given. If both hindlimbs were fully clasped and touching the abdomen, a score of
1156 3 was assigned.
1157
1158 *Grip strength.* For the grip strength test, forelimb, hindlimb, and 4-limbs grip strength was
1159 evaluated using a grip strength meter (Bioseb). Animals were held by the tail and allowed to place
1160 forelimbs on the bar, or they were restrained to place hindlimbs on the bar connected to the force
1161 sensor. Mice were slowly pulled away until they released the bar, and the maximal grip force
1162 measured during the pulling session was recorded. For the 4-limb measurement, using a mesh
1163 pull bar attachment, animals were handled by the tail so that all the paws latched onto the mesh

1164 pull the bar together. The mice were slowly and steadily pulled away from the apparatus exactly
1165 parallel from the countertop until paws were released from the mesh. A modified version of the
1166 forelimb grip strength test was performed as previously described[12]. Briefly, the meter was rotated
1167 vertically and the measurement procedure was identical to the conventional test, except for the
1168 direction in which the mouse's tail was pulled. Each animal's grip strength (in *g*) was recorded,
1169 and data from five trials were collected.
1170
1171 *Pole test.* Motor coordination and balance with striatal involvement was assessed with the vertical
1172 pole test, which consisted of a plastic pole (50 cm high, diameter 1 cm) placed vertically on a
1173 mouse cage. Mice were individually placed at the top of the pole facing upward by their front paws
1174 on the pole, and the time taken to turn around and climb down the pole was recorded. A maximum
1175 time of 120 s was given to complete the task. If the mouse fell from the top of the pole, a time of
1176 120 s was recorded. Each mouse underwent three trials, and the pole was cleaned with 70%
1177 ethanol between animals. Data from three trials were averaged for each mouse.
1178
1179 **qPCR**
1180 After rapid dissection of the hippocampus, tissue was preserved in RNAlater (Invitrogen)
1181 overnight at 4°C before storing at −80°C until use. Hippocampal RNA was extracted according to
1182 the manufacturer's instructions using a RNeasy Mini Kit (Qiagen). Quality and concentration of
1183 total RNA were measured on the Nanodrop 8000 (Thermo Fisher). cDNA was subsequently
1184 synthesized with SuperScript III (Invitrogen), following the manufacturer's recommendations.
1185 Samples were mixed with SYBR Green master mix (Thermo Fisher) and primers for *Mmp2* (FW:
1186 5'-CAAGTTCCCCGGCGATGTC-3'; REV: 5'-TTCTGGTCAAGGTCACCTGTC-3') before loading
1187 as technical replicates for qPCR on a QuantStudio 7 Flex Real-Time PCR System (Thermo
1188 Fisher). Cycle counts for mRNA quantification were normalized to *Rplp0* (FW: 5'-
1189 AGATTCGGGATATGCTGTTGGC-3'; REV: 5'-CCAGTTGGTAACAATGCCATGT-3'). The ΔΔCT

1190 method was used to provide gene expression values, and expression levels were normalized to
1191 *Rplp0*.
1192
1193 **Western blotting**
1194 For Western blotting of MMP2 or TIMP2 within hippocampus, dissected hippocampi were
1195 manually homogenized with 60 strokes in RIPA lysis buffer (Thermo Fisher), with protease
1196 inhibitors (Roche), before centrifugation at 20,000g for 25 min at 4°C. Protein concentration of the
1197 supernatant was determined using the BCA kit (Thermo Fisher). Samples with equal amounts of
1198 protein were separated on 4-12% NuPAGE Bis-Tris precast denaturing gels (Invitrogen) and
1199 transferred onto nitrocellulose membranes (BioRad, Hercules, CA, USA) at 125 V for 90 min.
1200 Membranes were blocked with 3% milk-TBST (0.125% Tween) for 1 hour at room temperature
1201 and then probed with primary antibodies diluted in 3% milk-TBST solution overnight at 4°C: anti-
1202 TIMP2 (1:500; #D18B7, Cell Signaling), anti-MMP2 (1:1000; #ab86607, Abcam), and anti-actin
1203 (1:10000; #A5060, Sigma). Membranes were washed and probed with horseradish-peroxidase-
1204 conjugated anti-mouse (1:15,000; #1705047, BioRad) or anti-rabbit (1:15,000; #1705046,
1205 BioRad) for 1 hour at room temperature. Membranes were developed using ECL Clarity reagent
1206 (BioRad) and imaged using ChemiDoc MP Imaging System and Image Lab software (BioRad).
1207 Band intensities were quantified using ImageJ software as described previously[13].
1208 For TIMP2 detection in ISF samples, 4 consecutive baseline eISF samples from microdialysis
1209 were pooled and concentrated ~6 fold using Amicon Ultra Centrifugal Filters (3 kDa Ultracel, 0.5
1210 mL, Millipore). Concentrated samples were then processed for western blotting as described
1211 above. Estimation of exchangeable interstitial fluid (eISF) TIMP2 protein levels were determined
1212 by extrapolation from a standard curve of recombinant mouse TIMP2 (R&D/Biotechne) ranging
1213 from 0.31 ng to 20 ng run alongside ISF samples in SDS-PAGE/Western that had been
1214 concentrated ~9.2-fold.
1215

Supplementary Figure 1

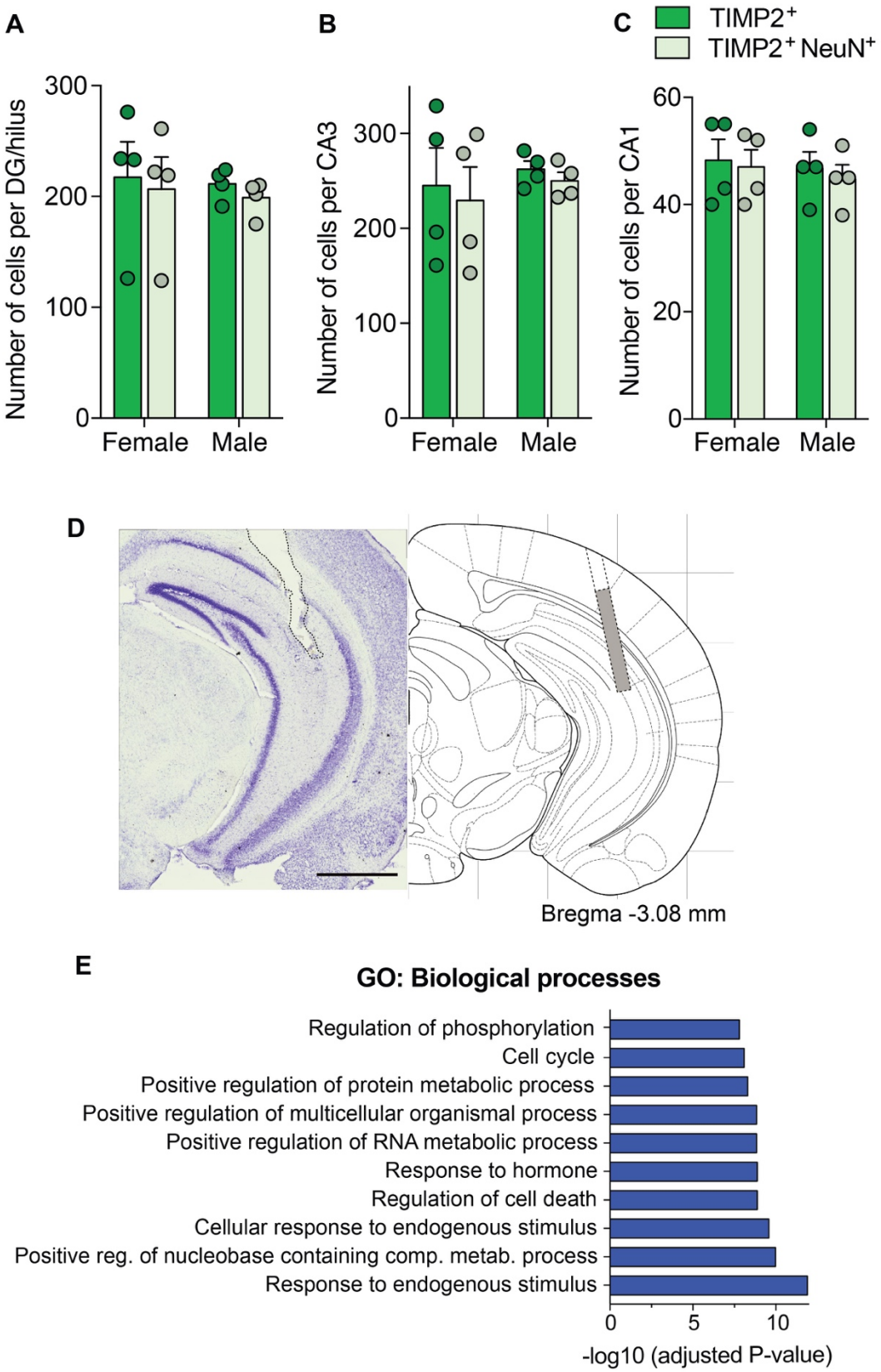

1239 **Supplementary Figure 1. TIMP2 protein is found in hippocampal neurons in male and**
1240 **female mice, and its loss affects hippocampal transcriptome.**
1241 **(A)** Quantification of the total number of TIMP2$^+$ and TIMP2$^+$ NeuN$^+$ cells at the hilus/DG, **(B)** CA3
1242 and **(C)** CA1 subregions of the hippocampus from WT males and females at 2 months of age (N
1243 = 4 mice per sex). **(D)** Cresyl violet-stained section depicting the microdialysis probe tract through
1244 brain surface extending into hippocampus, with microdialysis probe position seen at Bregma -
1245 3.08mm based on Paxinos and Watson atlas. Scale bar, 500 μm. **(E)** Top 10 significant pathways
1246 for upregulated DEGs in hippocampi of TIMP2 KO mice relative to WT mice (N = 13-17 mice per
1247 group). Data are represented as mean ± SEM.
1248
1249
1250
1251
1252
1253
1254
1255
1256
1257
1258
1259
1260
1261
1262
1263
1264

1265 **Supplementary Figure 2**

1266

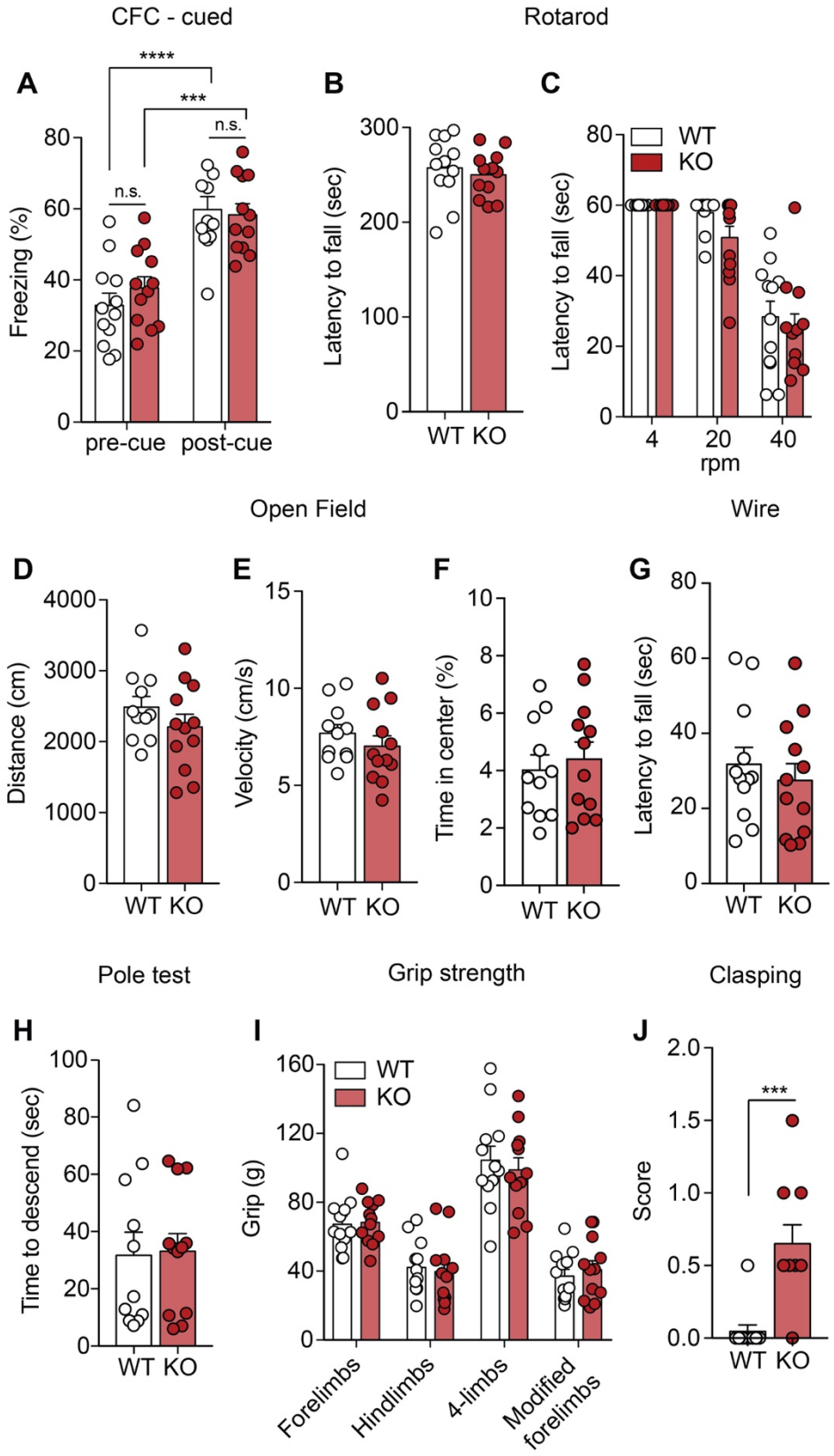

1267 **Supplementary Figure S2. Loss of TIMP2 does not affect amygdala-associated behavior or**
1268 **overall motor function.**
1269 **(A)** Percentage of freezing detected in the cued task of the fear-conditioning assay in WT and
1270 TIMP2 KO mice (2-3 months of age, N = 12 mice per group). **(B)** Latency of TIMP2 KO and WT
1271 mice to fall in the rotarod in the fixed and **(C)** acceleration protocol at 4, 20 and 40 rpm (N = 12
1272 mice per group). **(D)** Total distance traveled by TIMP2 KO and WT mice in the open field, as well
1273 as **(E)** velocity, and **(F)** percentage of time spent in the center of the arena (N = 11-12 mice per
1274 group). **(G)** Latency of TIMP2 KO and WT mice to fall in the wire test (N = 12 mice per group). **(H)**
1275 Time for TIMP2 KO and WT mice to descend the pole in the pole test (N = 11-12 mice per group).
1276 **(I)** Grip strength of the fore-, hind- and four limbs in TIMP2 KO and WT mice (N = 12 mice per
1277 group). **(J)** Hindlimb extension by clasping score in TIMP2 KO and WT mice (N = 10-11 mice per
1278 group). Data are represented as mean ± SEM. Student's *t*-test for two-group comparisons. n.s.,
1279 not significant.
1280
1281
1282
1283
1284
1285
1286
1287
1288
1289
1290
1291
1292

1293 **Supplementary Figure 3**

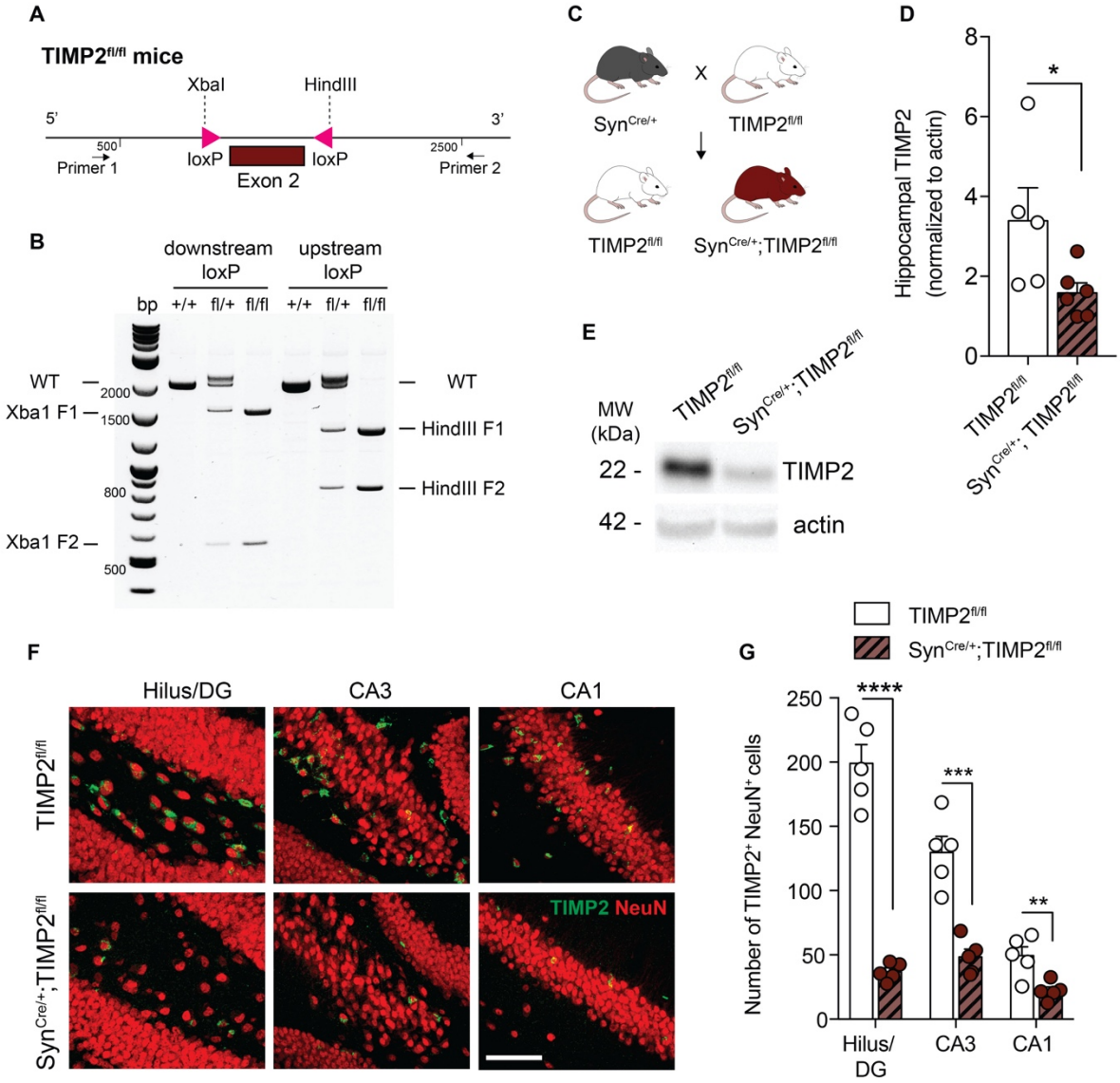

1294

1295 **Supplementary Figure 3. Creation of a conditional model to target neuronal pools of TIMP2.**
1296 **(A)** Schematic illustration of the targeting strategy of to insert loxP sites flanking exon 2 to
1297 generate a model for conditional deletion of *TIMP2*. **(B)** Representative genotyping results
1298 revealing the PCR products for the mutant LoxP and wild-type alleles. Wild-type (+/+),
1299 heterozygous (fl/+), and homozygous (fl/fl) mice were identified according to this strategy. **(C)**
1300 Schematic diagram of cross-breeding strategy to establish neuron-specific TIMP2 deletion: male
1301 $TIMP2^{fl/fl}$ mice were mated with $Syn^{Cre/+}$ females to obtain $Syn^{Cre/+}$; $TIMP2^{fl/fl}$ and their respective
1302 $TIMP2^{fl/fl}$ littermate controls. **(D-E)** Representative TIMP2 immunoblot and corresponding
1303 quantification of TIMP2 protein levels from hippocampal lysate of $TIMP2^{fl/fl}$ and $Syn^{Cre/+}$; $TIMP2^{fl/fl}$
1304 (2-3 months of age, N = 5-6 mice per group). **(F)** High-magnification view of hilus/DG, CA3, and
1305 CA1 sub-regions of TIMP2+ cells co-expressing NeuN in $TIMP2^{fl/fl}$ and $Syn^{Cre/+}$; $TIMP2^{fl/fl}$ mice (2-
1306 3 months of age, N = 5 mice per group, scale bar, 20 μm) with corresponding **(G)** quantification
1307 of the total number of $TIMP2^{+}$ cells with $NeuN^{+}$ nuclei across hippocampal subregions. Data are
1308 represented as mean ± SEM. Student's t-test for two-group comparisons. *P<0.05, **P<0.01,
1309 ***P<0.001, ****P<0.0001. Data points represent individual mice.
1310
1311
1312
1313
1314
1315
1316
1317
1318
1319
1320

Supplementary Figure 4

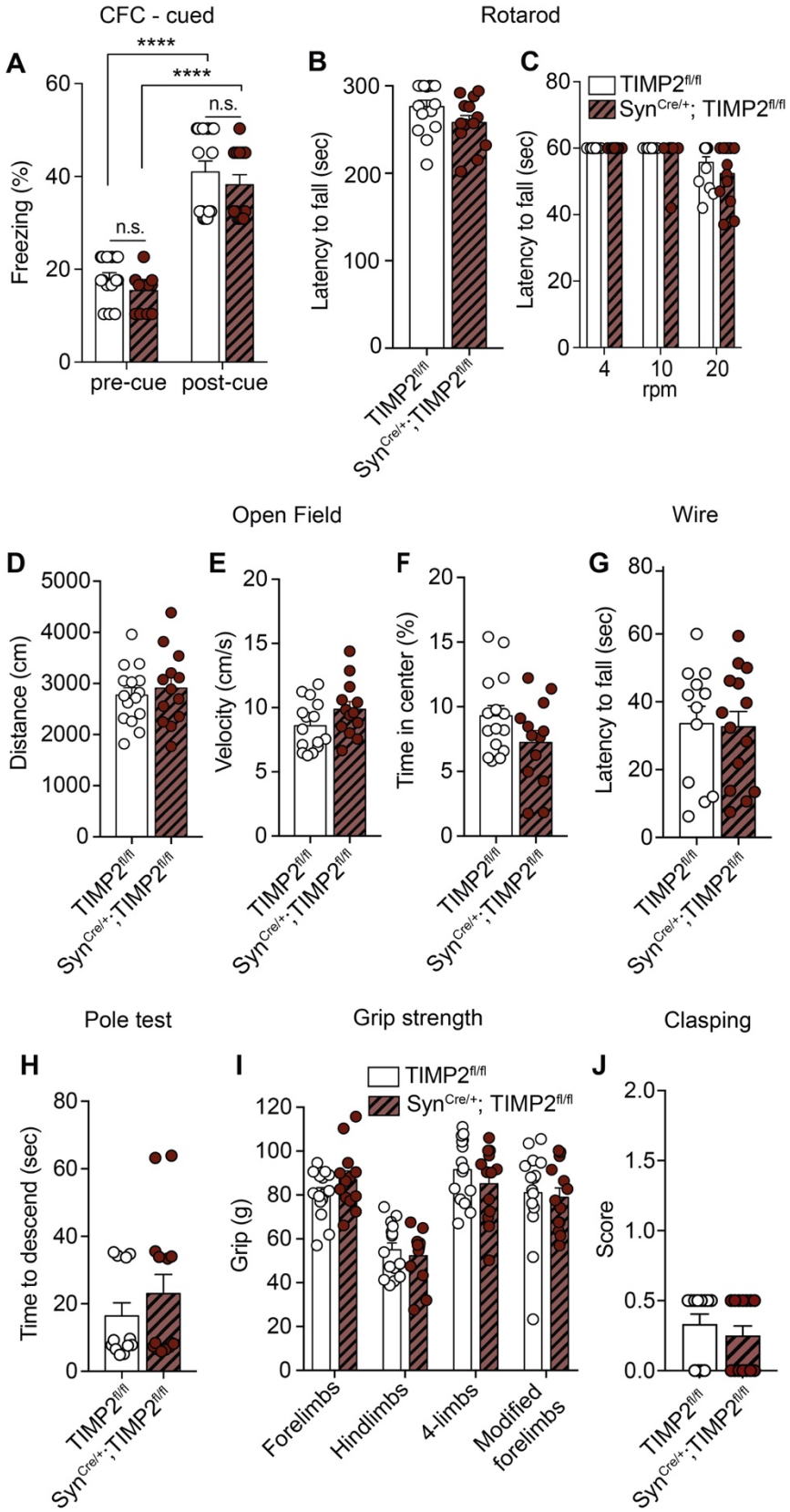

1346 **Supplementary Figure 4. Neuronal TIMP2 deletion does not impair amygdala-associated**
1347 **behavior or overall motor function.**
1348 **(A)** Percentage of freezing detected in the cued task of the fear-conditioning assay in $TIMP2^{fl/fl}$
1349 and $Syn^{Cre/+}$; $TIMP2^{fl/fl}$ mice (2-3 months of age, N = 13-15 mice per group). **(B)** Latency of
1350 $TIMP2^{fl/fl}$ and $Syn^{Cre/+}$; $TIMP2^{fl/fl}$ mice to fall in the rotarod in the fixed and **(C)** acceleration protocol
1351 at 4, 10 and 20 rpm (N = 13-15 mice per group). **(D)** Total distance traveled by $TIMP2^{fl/fl}$ and
1352 $Syn^{Cre/+}$; $TIMP2^{fl/fl}$ mice in the open field, as well as **(E)** velocity, and **(F)** percentage of time spent
1353 in the center of the arena (N = 13-15 mice per group). **(G)** Latency of $TIMP2^{fl/fl}$ and $Syn^{Cre/+}$;
1354 $TIMP2^{fl/fl}$ mice to fall in the wire test (N = 12-14 mice per group). **(H)** Time for $TIMP2^{fl/fl}$ and $Syn^{Cre/+}$;
1355 $TIMP2^{fl/fl}$ mice to descend the pole in the pole test (N = 12-14 mice per group). **(I)** Grip strength of
1356 the fore-, hind- and four limbs in $TIMP2^{fl/fl}$ and $Syn^{Cre/+}$; $TIMP2^{fl/fl}$ mice (N = 13-15 mice per group).
1357 **(J)** Hindlimb extension by clasping score in $TIMP2^{fl/fl}$ and $Syn^{Cre/+}$; $TIMP2^{fl/fl}$ mice (N = 12-14 mice
1358 per group). Data are represented as mean ± SEM. Student's *t*-test for two-group comparisons.
1359 n.s., not significant.
1360
1361

1362 **Supplementary References**

1363

1364 1. Gu B, Posfai E, Rossant J. Efficient generation of targeted large insertions by
1365 microinjection into two-cell-stage mouse embryos. *Nat Biotechnol* 2018; **36**(7)**:** 632-637.
1366

1367 2. Zhu Y, Romero MI, Ghosh P, Ye Z, Charnay P, Rushing EJ *et al.* Ablation of NF1 function
1368 in neurons induces abnormal development of cerebral cortex and reactive gliosis in the
1369 brain. *Genes Dev* 2001; **15**(7)**:** 859-876.
1370

1371 3. Ulrich JD, Burchett JM, Restivo JL, Schuler DR, Verghese PB, Mahan TE *et al.* In vivo
1372 measurement of apolipoprotein E from the brain interstitial fluid using microdialysis. *Mol*
1373 *Neurodegener* 2013; **8:** 13.
1374

1375 4. Castellano JM, Mosher KI, Abbey RJ, McBride AA, James ML, Berdnik D *et al.* Human
1376 umbilical cord plasma proteins revitalize hippocampal function in aged mice. *Nature* 2017;
1377 **544**(7651)**:** 488-492.
1378

1379 5. Nguyen PT, Dorman LC, Pan S, Vainchtein ID, Han RT, Nakao-Inoue H *et al.* Microglial
1380 Remodeling of the Extracellular Matrix Promotes Synapse Plasticity. *Cell* 2020; **182**(2)**:**
1381 388-403 e315.
1382

1383 6. Ippolito DM, Eroglu C. Quantifying synapses: an immunocytochemistry-based assay to
1384 quantify synapse number. *J Vis Exp* 2010; (45).
1385

1386 7. Jacot-Descombes S, Keshav NU, Dickstein DL, Wicinski B, Janssen WGM, Hiester LL *et*
1387 *al.* Altered synaptic ultrastructure in the prefrontal cortex of Shank3-deficient rats. *Mol*
1388 *Autism* 2020; **11**(1)**:** 89.
1389
1390 8. De Waele J, Reekmans K, Daans J, Goossens H, Berneman Z, Ponsaerts P. 3D culture
1391 of murine neural stem cells on decellularized mouse brain sections. *Biomaterials* 2015;
1392 **41:** 122-131.
1393
1394 9. Tajerian M, Hung V, Nguyen H, Lee G, Joubert LM, Malkovskiy AV *et al.* The hippocampal
1395 extracellular matrix regulates pain and memory after injury. *Mol Psychiatry* 2018; **23**(12)**:**
1396 2302-2313.
1397
1398 10. Mateus-Pinheiro A, Alves ND, Patricio P, Machado-Santos AR, Loureiro-Campos E, Silva
1399 JM *et al.* AP2gamma controls adult hippocampal neurogenesis and modulates cognitive,
1400 but not anxiety or depressive-like behavior. *Mol Psychiatry* 2017; **22**(12)**:** 1725-1734.
1401
1402 11. Zhu JW, Li YF, Wang ZT, Jia WQ, Xu RX. Toll-Like Receptor 4 Deficiency Impairs Motor
1403 Coordination. *Front Neurosci* 2016; **10:** 33.
1404
1405 12. Takeshita H, Yamamoto K, Nozato S, Inagaki T, Tsuchimochi H, Shirai M *et al.* Modified
1406 forelimb grip strength test detects aging-associated physiological decline in skeletal
1407 muscle function in male mice. *Sci Rep* 2017; **7:** 42323.
1408
1409 13. Castellano JM, Kim J, Stewart FR, Jiang H, DeMattos RB, Patterson BW *et al.* Human
1410 apoE isoforms differentially regulate brain amyloid-beta peptide clearance. *Sci Transl Med*
1411 2011; **3**(89)**:** 89ra57.